CYCLOCIM: A 4-D variational assimilation system for the climatological mean seasonal cycle of the ocean circulation

Qian Huang[1], François Primeau[1], Tim Devries[b]

[a]*Department of Earth System Science, University of California, Irvine, CA, United States*
[b]*Department of Geography, University of California, Santa Barbara, CA, United States*

Abstract

We describe a new 4-D variational assimilation system, called CYCLOCIM, to estimate the climatological seasonal cycle of the residual mean ocean circulation. CYCLOCIM assimilates monthly mean potential temperature and salinity data from the World Ocean Atlas, and CFC-11, CFC-12 and natural radiocarbon measurements for the deep ocean from the Global Data Analysis Project, Version 2. CYCLOCIM's control parameters include: (i) a seasonally varying 3-D field of unresolved eddy-stress divergences that appear in the horizontal momentum equations, (ii) seasonally varying 2-D correction fields for the surface heat and freshwater fluxes, and (iii) a constant scaling factor for the air-sea flux of CFCs. The influence of initial conditions on a fully spun-up ocean model vanishes. Thus, unlike other 4-D variational assimilation systems, CYCLOCIM does not include initial conditions as control parameters. A Bayesian procedure is used to formulate the inverse problem, which is solved by finding the maximum of the posterior probability distribution. The optimization process used to find the maximum includes a forward simulation to calculate the flow velocities and tracer distributions followed by a backward ("adjoint") simulation to compute the gradient of the posterior. A quasi-Newton search algorithm is used to find the set of parameters to maximize the posterior probability. We find that by resolving the seasonal cycle the model is able to better fit the observations in the upper ocean compared to a previous steady-state version of the model. The main output from CYCLOCIM is a set of 12 data-constrained monthly tracer transport matrices that will provide a useful circulation model for global marine biogeochemical cycle studies.

Keywords:

1. Introduction

An important goal of data assimilation in oceanography is to provide an estimate of the state of the ocean that is consistent with available observations and known physical laws. Variational assimilation methods aim to achieve this goal by iteratively minimizing an objective function that measures the difference between predictions obtained from a dynamical circulation model and available observations (Ghil and Malanotte-Rizzoli, 1991). While the applications for global data-assimilation products are numerous, the detection of climate trends is major driving motivation. Typically, the inputs to the objective function are the model's initial conditions and surface boundary conditions for the fluxes of heat, freshwater, and momentum, but sometimes internal eddy-diffusivity parameters are also used (e.g. Balmaseda et al., 2015; Köhl, 2015; Forget et al., 2015; Osafune et al., 2015; Fukumori et al., 2018).

In addition to producing a space-time interpolation of the sparse and irregulary sampled observations, a 4-D variational assimilation system also produces an estimate of the global circulation. The resulting estimate of the circulation can be extremely useful for computing tracer flux divergences in biogeochemical applications. When the focus is on recent trends and variability that fall within the assimilation period, the estimated circulation can be used unambiguously (e.g Brix et al., 2015; Doi et al., 2015; Carroll et al., 2020). For applications involving the functioning of biogeochemical cycles on longer timescales, one can time-average the estimate and assume that the resulting average is representative of the long-term mean circulation. For example, Graven et al. (2012) average the state estimate for the period 1992-2004 from the ECCO-GODAE assimilation system (Stammer et al., 2004), into monthly mean tracer transport matrices, which are then used to simulate the pre-industrial carbon cycle and its transient evolution for 1760-2007. For this they assume a climate system that is stationary to first order and repeatedly cycle through the same 12 tracer transport matrices. However, because each iteration of the assimilation procedure simulates the circulation for at most a few decades while repeatedly adjusting the initial conditions, the resulting circulation is never fully spun-up. Consequently, it is not clear that the circulation, especially in the deep ocean, produces stable water

masses when the circulation is extrapolated to time-scales longer than those used for the assimilation. Indeed, Graven et al. (2012) demonstrate the existence of clear biases in the shallow-to-deep exchange of water masses in the data-assimilation circulation from the ECCO-GODAE model. Similarly, Liu et al. (2012) show that even after optimizing the initial conditions, the surface forcing, and eddy-diffusivities, the German ECCO synthesis (GECCO) has temperature errors that are several times bigger than their prior estimates.

For biogeochemistry research that requires tracer simulations that are much longer than the observational record an alternative data-assimilation procedure has been developed (e.g. Schlitzer, 2007; DeVries and Primeau, 2011). It aims to directly constrain a steady-state model of the ocean's long-term climatological mean using a 3-D (no time-dependence) variational assimilation procedure. The application of inverse methods to global marine biogeochemical cycles has progressed rapidly in recent years because of the development of such a data-constrained steady model expressed in the form of a tracer transport matrix (e.g. Devries et al., 2012; DeVries et al., 2013; Holzer and Primeau, 2013; Devries and Deutsch, 2014; DeVries, 2014; Holzer et al., 2014; Teng et al., 2014; Frants et al., 2015; Holzer et al., 2016; Weber et al., 2016; DeVries et al., 2017; Pasquier and Holzer, 2016; Roshan et al., 2017; Pasquier and Holzer, 2017; Roshan and DeVries, 2017; Holzer et al., 2017; John et al., 2018; Wang et al., 2019; Martin et al., 2019a,b). The tracer transport matrix used in the aforementioned studies is produced by a data assimilation system known as the Ocean Circulation Inverse Model (OCIM) (DeVries and Primeau, 2011; Primeau et al., 2013; DeVries, 2014; DeVries and Holzer, 2019). OCIM uses a variational method to assimilate stationary and transient tracers into a steady-state model for the large-scale momentum balance of the ocean. Because of the assimilation process, the circulation biases found in most prognostic ocean general circulation models (OGCMs) are greatly reduced. As a result, biogeochemical inferences made on the basis of tracer flux divergences computed using OCIM can be interpreted more reliably than those obtained from free running OGCMs.

The steady-state assumption used in the OCIM system makes it possible to obtain a fully-spun up ocean state by direct matrix inversion rather than by a slow time-stepping spin-up as is used in traditional OGCMs. This capability makes it feasible to compute the $\mathcal{O}(10^3)$ iterations of the forward and adjoint model runs that are required by the iterative numerical optimization algorithm to bring the model state into agreement with the tracer-data constraints.

An important drawback of the steady-state formulation is that it ignores the pronounced seasonality of ventilation processes in mid- to high-latitudes (e.g. Marshall and Schott, 1999; Williams et al., 1995). This neglect can lead to potentially important biases whose influence on biogeochemial inferences are difficult to quantify. For example, it is well known that late-winter mixed layer water properties are preferentially selected for export to the permanent pycnocline (e.g. Stommel, 1979; Williams et al., 1995). By neglecting the seasonal cycle, the OCIM tracer-transport operator must necessarily be biased in the upper ocean if it is to reproduce the correct water-mass properties in the permanent thermocline and abyssal waters (see for example the discussion in Yu and Malanotte-Rizzoli, 1996, 1998).

Here we present an extended OCIM assimilation system, which we call CYCLOCIM, that produces a cyclo-stationary state estimate for the climatological seasonally varying ocean circulation. The direct matrix inversions via LU factorization that were used to obtain fully spun-up steady states in OCIM are replaced by calls to a cyclo-stationary Newton-Krylov solver (e.g. Li and Primeau, 2008; Bardin et al., 2014). Compared with the majority of existing ocean reanalysis efforts (e.g. Mazloff et al., 2010; Balmaseda et al., 2015; Köhl, 2015; Forget et al., 2015; Osafune et al., 2015; Fukumori et al., 2018), what sets our system appart is that it aims to estimate the ocean's mean annual cycle rather than its inter-annual variability. CYCLOCIM is therefore a generalization to a periodic annual cycle of previous steady-state inversions (e.g. Schlitzer, 1993; Wunsch, 1996; Ganachaud and Wunsch, 2000; Schlitzer, 2007; DeVries and Primeau, 2011). The goal of the CYCLOCIM assimilation system is therefore most similar to the one in the study of Wenzel et al. (2001) who developed a 4-D variational assimilation method to estimate a cyclo-stationary annual cycle of the ocean circulation. There are, however, some important methodological differences. Most importantly, Wenzel et al. (2001) follow Yu and Malanotte-Rizzoli (1998) by adding a penalty term for departures from a cyclo-stationary state to the usual cost function that measures the misfit between the model and the observations. They then use the initial conditions (i.e. the January model state) along with the monthly mean surface forcing as the control variables in the minimization problem. The data-assimilation procedure used in Wenzel et al. (2001) can therefore be viewed as trading off model-data misfits for a reduced temporal drift. Indeed, in a fully spun-up model with zero drift, the initial conditions exert no controllability on the objective function. In contrast, CYCLOCIM searches for the optimal state in the space of perfectly cyclo-

stationary model solutions that have zero temporal drift. This is achieved by adding time-periodic eddy-stress divergence terms to the horizontal momentum equations and using them as control variables in the optimization of the residual mean circulation. In this respect CYCLOCIM follows the pioneering study of Ferreira et al. (2005) who added eddy-stresses to initial conditions and surface forcing as the control variables used to minimize solution drift and departures from climatological observations of temperature. In CYCLOCIM we completely eliminate the initial conditions from the list of adjustable parameters by directly solving for the cyclo-stationary annual cycle. This cyclo-stationary solution represents the projection of the ocean's long-term climatological attractor onto a periodic annual cycle.

The primary focus of this article is to document the numerical formulation of the model and the solution method rather than presenting a scientifically usable state estimate. In Section 2 we present the governing equations for the residual mean circulation and the computational method used to obtain their cyclo-stationary solution. In Section 3 we present the governing equations and solution method for the cyclo-stationary and transient tracers that are used to constrain the circulation. In Section 4 we give a Bayesian formulation of the inverse problem. We then present how we use the adjoint method to efficiently compute the gradient of the logarithm of the posterior probability density function so that we can locate the maximum of the posterior probability function. In Section 5 we compare the tracers simulated using our most probable model to observations. We show the most probable meridional overturning circulation conditioned on the tracer data, along with the implied meridional fluxes of heat and fresh water. Finally, in Section 6 we summarize the results and give directions for future model developments and applications.

2. Dynamical model

The dynamical model is based on the linearized Navier-Stokes equations with hydrostatic and Boussinesq approximations with an implicit free surface,

$$
\begin{aligned}
u^\dagger_t - fv^\dagger + \frac{1}{a\cos\phi} g\eta_\lambda + \mathcal{D}u^\dagger &= -\frac{1}{a\cos\phi}\frac{p_\lambda}{\rho_0} + \frac{\delta_{1k}}{\Delta z_1}\frac{\tau^\lambda + \delta\tau^\lambda}{\rho_0} + \frac{1}{\rho_0}\tau^{e\lambda}_z, \quad (a)\\
v^\dagger_t + fu^\dagger + \frac{1}{a} g\eta_\phi + \mathcal{D}v^\dagger &= -\frac{1}{a}\frac{p_\phi}{\rho_0} + \frac{\delta_{1k}}{\Delta z_1}\frac{\tau^\phi + \delta\tau^\phi}{\rho_0} + \frac{1}{\rho_0}\tau^{e\phi}_a, \quad (b)\\
p &= g\int_z^0 \rho(z^{'})dz^{'}, \quad (c)\\
\frac{1}{a\cos\phi}[(v^\dagger\cos\phi)_\phi + u^\dagger_\lambda] + w^\dagger_z &= 0, \quad (d)\\
\eta_t + \int_{z_{bot}(\lambda,\phi)}^0 \left\{\frac{1}{a\cos\phi}[(v^\dagger\cos\phi)_\phi] + u^\dagger_\lambda\right\} dz &= 0, \quad (e)
\end{aligned}
\tag{1}
$$

where $(u^\dagger, v^\dagger, w^\dagger)$ is the residual mean velocity rather than the Eulerian mean; $\vec{\tau} = (\tau^\lambda, \tau^\phi)$ is the wind-stress and the factor $\delta_{1k}/\Delta z_1$ is used to indicate that the wind stress is applied as a body force in the top layer of the discretized model; $\vec{\tau}^e = \left(\tau^{e\lambda}, \tau^{e\phi}\right)$ is a cyclo-stationary eddy-stress vector; η is the seasonally-varying mean dynamic topography; p is the climatologically-averaged seasonally-varying baroclinic pressure computed using the hydrostatic balance and the observed climatological density field; ρ is the climatologically-averaged seasonally-varying density; $\delta\vec{\tau} = (\delta\tau^\lambda, \delta\tau^\phi)$ is a correction to the prescribed wind-stress climatology (e.g. Stammer et al., 2002; Ferreira et al., 2005; DeVries and Primeau, 2011); f is the Coriolis parameter; g is gravity. λ is the longitude and ϕ is the latitude. The continuity equation is solved in a domain with the surface set at $z = 0$ and a spatially variable bottom topography, $z_{bot}(\lambda, \phi)$, i.e we assume that $|\eta| \ll -z_{bot}(\lambda, \phi)$. The friction operator, $\mathcal{D}$, is here taken to be a simple Rayleigh drag, i.e. $\mathcal{D}(u^\dagger, v^\dagger) = r(u^\dagger, v^\dagger)$, $r = 10^{-6}$ s^{-1}. As previously mentioned, the averaging operator used to define the residual mean is based on a projection of the ocean circulation on its cyclo-stationary mean seasonal-cycle. Consequently, any deviation from this perfectly periodic state is, by definition, part of the "eddy" field. This is different from conventional 4-D variational assimilation models where the large-scale low-frequency variability such as ENSO is explicitly resolved by the model and does not part of the "eddy" field.

Rewriting (1) in matrix-vector form we have

$$\partial_t \begin{bmatrix} u^\dagger \\ v^\dagger \\ w^\dagger \\ \eta \end{bmatrix} + \boldsymbol{\mathcal{M}} \begin{bmatrix} u^\dagger \\ v^\dagger \\ w^\dagger \\ \eta \end{bmatrix} = \mathcal{F} + \mathcal{F}^e, \tag{2}$$

where

$$\boldsymbol{\mathcal{M}} = \begin{bmatrix} r & -f & 0 & \frac{1}{a\cos\phi} g\partial_\lambda \\ f & r & 0 & \frac{1}{a} g\partial_\phi \\ \frac{1}{a\cos\phi}\partial_\lambda & \frac{1}{a\cos\phi}\partial_\phi \cos\phi & \partial_z & 0 \\ \partial_z^{-1}\partial_\lambda & \partial_z^{-1}\partial_\phi \cos\phi & 0 & 0 \end{bmatrix}, \tag{3}$$

with the linear operator ∂_z^{-1} defined to return the indefinite vertical integral of its operand, i.e. $\partial_z^{-1} q \equiv \int_z^0 q dz$. The forcing term on the right hand side is decomposed into two periodic forcing terms, $\mathcal{F}(t + \Delta T) = \mathcal{F}(t)$ and $\mathcal{F}^e(t + \Delta T) = \mathcal{F}^e(t)$. The first contribution consists of the wind-stress and the baroclinic pressure forces,

$$\mathcal{F}(t) \equiv \frac{1}{\rho_0} \begin{bmatrix} \frac{\delta_{1k}}{\Delta z_1}\tau^\lambda - \frac{g}{a\cos\phi}\partial_\lambda \partial_z^{-1}\rho \\ \frac{\delta_{1k}}{\Delta z_1}\tau^\phi - \frac{g}{a}\partial_\phi \partial_z^{-1}\rho \\ 0 \\ 0 \end{bmatrix}, \tag{4}$$

which can be computed directly from the observed climatological wind-stress obtained from the European Centre for Medium-Range Weather Forecasts (ECMWF) climatological fields (Trenberth et al., 1989), and the observed climatological density computed using the equation of state for seawater and the World Ocean Atlas 2013 (Boyer et al., 2013) gridded temperature and salinity fields. The second contribution consists of the unobserved errors in the wind-stress climatology and the unresolved eddy-stress forcing

$$\mathcal{F}^e = \frac{1}{\rho_0} \begin{bmatrix} \frac{\delta_{1k}}{\Delta z_1}\delta\tau^\lambda + \partial_z \tau^{e\lambda} \\ \frac{\delta_{1k}}{\Delta z_1}\delta\tau^\phi + \partial_z \tau^{e\phi} \\ 0 \\ 0 \end{bmatrix}, \tag{5}$$

which will be inferred via the Bayesian inversion procedure using transient and cyclo-stationary tracer observations. We do not attempt to separate the contribution of the wind-stress correction (here applied as a body force in

the upper-most layer of the model) and the eddy-stress divergence. Only their sum appears in the model and they are therefore lumped together in the inversion.

2.1. Space discretization

The dynamical state of the model is discretized using a staggered Arakawa B-grid finite-difference scheme (e.g. Haltiner and Williams, 1980) with a uniform $4^\circ \times 4^\circ$ horizontal resolution and a vertical discretization with 24 layers whose thicknesses increase monotonically with depth (Table 1) resulting in a discretized dynamical state vector $\boldsymbol{x} = [u^\dagger, v^\dagger, w^\dagger, \eta]$ expressed as a $122\,333 \times 1$ matrix. With this discretization scheme, the operator $\boldsymbol{\mathcal{M}}$ becomes a time-independent $122\,333 \times 122\,333$ sparse-matrix operator. Similarly, the right-hand-side forcings, $\mathcal{F}$ and $\mathcal{F}^e$ become time-periodic 122 333-dimensional vectors, $\mathbf{F}$ and $\mathbf{F}^e$. The resulting governing equation for the dynamics expressed in matrix-vector form is

$$\frac{d\boldsymbol{x}}{dt} + \mathbf{M}\boldsymbol{x} = \mathbf{F}(t) + \mathbf{F}^e(t). \tag{6}$$

Following DeVries (2014), we also added a discretized horizontal Laplacian operator with a diffusivity of 10^{-3} m^2/s to the part of the $\mathbf{M}$ operator corresponding to the equation for η, i.e. equation (1e). This was done to damp out a checkerboard computational mode associated with the B-grid discretization.

36.1	37.3	40.7	46.3	54.2	64.4
76.8	91.5	108.4	127.6	149.1	172.8
198.7	227.0	257.5	290.2	325.2	362.5
402.0	443.8	487.8	534.1	582.7	633.5

Table 1: Vertical discretization used in CYCLOCIM. The thicknesses in meters increase monotonically with increasing depth.

2.2. Time discretization and cyclo-stationary state

Equation (6) can be further discretized in time using an Euler backward scheme with $dt = \Delta T/12$, to get

$$\begin{aligned} \mathbf{A}\boldsymbol{x}_n &= \boldsymbol{x}_{n-1} + (\mathbf{F}_n + \mathbf{F}^e_n)dt, \\ \mathbf{A} &\equiv \mathbf{I} + \mathbf{M}dt. \end{aligned} \tag{7}$$

with $\mathbf{F}_0 = \mathbf{F}_{12}$, $\mathbf{F}_0^e = \mathbf{F}_{12}^e$, and $\boldsymbol{x}_0 = \boldsymbol{x}_{12}$. Because the forcing term on the right-hand-side is periodic in time the fully spun-up dynamical state will be cyclo-stationary and satisfy the following block-matrix system

$$\underbrace{\begin{bmatrix} -\mathbf{I} & \mathbf{A} & 0 & \cdots & 0 \\ 0 & -\mathbf{I} & \mathbf{A} & \cdots & 0 \\ \vdots & & \ddots & \ddots & \vdots \\ 0 & 0 & \cdots & -\mathbf{I} & \mathbf{A} \\ \mathbf{A} & 0 & \cdots & 0 & -\mathbf{I} \end{bmatrix}}_{\tilde{\mathbf{A}}} \begin{bmatrix} \boldsymbol{x}_{12} \\ \boldsymbol{x}_1 \\ \boldsymbol{x}_2 \\ \vdots \\ \boldsymbol{x}_{11} \end{bmatrix} = \begin{bmatrix} \mathbf{F}_1 + \mathbf{F}_1^e \\ \mathbf{F}_2 + \mathbf{F}_2^e \\ \vdots \\ \mathbf{F}_{11} + \mathbf{F}_{11}^e \\ \mathbf{F}_{12} + \mathbf{F}_{12}^e \end{bmatrix} dt. \tag{8}$$

The enormous size of the matrix, $\tilde{\mathbf{A}}$, precludes the use of a direct LU factorization to solve Eq. (8). We therefore obtain a solution to Eq. (8) using an iterative Newton-Krylov solver that avoids the need to explicitly construct $\tilde{\mathbf{A}}$. The convergence of the solver is greatly accelerated by the fact that it is possible to construct a nearly converged initial iterate using a Fourier representation of the continuous-time solution. Because $\mathbf{M}$ does not depend on t, a continous-time cyclo-stationary solution to Eq. (6) can be efficiently computed by first transforming the equation to Fourier space. To this end, we expand the forcing function and the solution in Eq. (6) into a truncated Fourier series with 6 complex sinusoidal modes

$$\begin{aligned} \mathbf{F}(t) + \mathbf{F}^e(t) &= \sum_{k=0}^{5} \widehat{\mathbf{F}}_k e^{ik2\pi t/\Delta T}, \\ \boldsymbol{x}(t) &= \sum_{k=0}^{5} \widehat{\boldsymbol{x}}_k e^{ik2\pi t\Delta T}, \end{aligned} \tag{9}$$

which transforms the coupled system of differential equations (6) into a system of 733 998 complex-valued algebraic equations

$$\begin{bmatrix} i\omega_0\mathbf{I} + \mathbf{M} & 0 & & 0 \\ 0 & i\omega_1\mathbf{I} + \mathbf{M} & 0 & \vdots \\ \vdots & 0 & \ddots & 0 \\ 0 & & 0 & i\omega_5\mathbf{I} + \mathbf{M} \end{bmatrix} \begin{bmatrix} \widehat{\boldsymbol{x}}_0 \\ \widehat{\boldsymbol{x}}_1 \\ \vdots \\ \widehat{\boldsymbol{x}}_5 \end{bmatrix} = \begin{bmatrix} \widehat{\mathbf{F}}_0 \\ \widehat{\mathbf{F}}_1 \\ \vdots \\ \widehat{\mathbf{F}}_5 \end{bmatrix}, \tag{10}$$

where the subscript corresponds to each sinusoidal mode in Eq.(9) and $\omega_k = k2\pi/\Delta T$. Because the matrix in Eq. (10) is block-diagonal it uncouples into

6 independent $122\,333 \times 122\,333$ systems, each of which can be solved using a complex sparse-matrix LU factorization. The resulting continuous-time solution can then be evaluated at $t = 0$ to construct an initial iterate

$$\boldsymbol{x}_1 = \Re \left\{ \sum_{k=0}^{5} \widehat{\boldsymbol{x}}_k \right\}, \tag{11}$$

for the Newton Krylov solver. Fully spun-up cyclo-stationary solutions can be obtained using this method with the equivalent of only a few years of simulation – typically 5 or less – without the need for a sophisticated pre-conditioner.

2.3. Choice of time step

Following Wenzel et al. (2001), we use a time step $dt = \Delta T/12$ in accordance with the time-resolution of the WOA climatology. Because our present goal is to describe the solution method rather than present a scientifically usable state estimate, we limit our presentation to the case of 12 time-steps per year. However, our assimilation method should work with an arbitrary number of time steps per year. We are planning a follow up paper in which we increase the horizontal resolution to $2^\circ \times 2^\circ$ and explore the sensitivity of the state estimate to the time-step size.

3. Tracer transport

The primary observational constraint for the CYCLOCIM state estimate consist of hydrographic tracer observations. The advection-diffusion equation for a tracer c is given by

$$\frac{\partial c}{\partial t} + \nabla \cdot [\boldsymbol{u}^\dagger(t) - \mathbf{K}(t)\nabla]c = \mathcal{S}(c,t), \tag{12}$$

where $\mathbf{K}(t)$ is the tracer diffusivity tensor and $\boldsymbol{u}^\dagger(t)$ is the residual mean circulation. The implicit averaging operator used to define the residual mean is based on a projection of the ocean circulation onto its climatological mean seasonal cycle. Thus both $\boldsymbol{u}^\dagger(t)$ and $\mathbf{K}(t)$ are assumed to be periodic functions with a period of $\Delta T = 1$ year.

For the particular state estimates we present here, the diffusivity tensor is constructed using an isopycnal diffusivity of 10^3 m^{2}s^{-1} and a vertical diffusivity of 10^{-5} m^{2}s^{-1}. (The sensitivity to this choice is explored briefly in

Appendix A.) The isopycnal surfaces were computed using the 2013 World Ocean Atlas (WOA2013) monthly-mean temperature and salinity (Boyer et al., 2013). In addition, the vertical diffusivity is enhanced to a value of 1 $\mathrm{m^2 s^{-1}}$ in a surface mixed layer of thickness h, which is prescribed according to the observed monthly-mean mixed layer depth climatology (de Boyer Montégut et al., 2004). This large value ensures that tracer concentrations are uniform within the surface mixed layer.

3.1. Space discretization

The tracer transport equations are discretized using a staggered Arakawa C-grid (e.g Haltiner and Williams, 1980). For the $4^\circ \times 4^\circ$ horizontal resolution with 24 vertical layers the model has a total of $N = 45\,515$ wet grid boxes. A discretized tracer field can then be organized into an $N \times 1$ column vector, $\boldsymbol{c}$. The discretized version of Eq.(12) can then be expressed in matrix-vector form as follows,

$$\frac{d\boldsymbol{c}}{dt} + \boldsymbol{\Gamma}(t)\boldsymbol{c} = \boldsymbol{s}(\boldsymbol{c}, t), \tag{13}$$

where $\boldsymbol{s}$ is an $N \times 1$ source vector and $\boldsymbol{\Gamma}(t)$ is a $N \times N$ sparse matrix constructed such that the matrix-vector product $\boldsymbol{\Gamma c}$ produces the advective-diffusive tracer flux divergence in each of the model's wet grid boxes. In the construction of $\boldsymbol{\Gamma}$, the diffusive tracer fluxes are discretized using second-order centered differences and the advective fluxes are discretized using a "Quick-up" scheme, that is, "semi-upwind" (i.e. the quadractic interpolation is biased towards the upstream direction) in the horizontal and "QUICK" in the vertical (Leonard, 1979). For the grid-box interfaces separating the ocean from the land or atmosphere, $\boldsymbol{\Gamma}$ is constructed to satisfy no normal flux conditions.

3.2. Potential temperature model

For the potential temperature equation the source term $\boldsymbol{s}$ appearing in Eq. (13) consists of a surface heat flux, which we model by restoring the temperature in the model's upper-most layer to a prescribed surface temperature field, $\boldsymbol{\theta}_a(t)$, that is periodic in time, i.e. $\boldsymbol{\theta}_a(t + \Delta T) = \boldsymbol{\theta}_a(t)$. With N_s wet surface grid-boxes, $\boldsymbol{s}$ can be expressed in matrix-vector form as

$$\boldsymbol{s} = \frac{1}{\tau}\boldsymbol{\Lambda}_s(\boldsymbol{\theta}_a - \boldsymbol{\Lambda}_s^T\boldsymbol{c}), \tag{14}$$

where $\tau = 30$ days (but see Appendix A.2 for sensitivity experiments), $\mathbf{\Lambda}_s$ is an $N \times N_s$ sparse matrix with ones on the main diagonal and zeros elsewhere. The state vector, $\boldsymbol{c}$, is organized such that its first N_s elements correspond to the surface values, therefore, $\mathbf{\Lambda}_s^T \boldsymbol{c}$ produces an $N_s \times 1$ vector of surface temperatures. The superscript T is used to denote the matrix transpose operation. The prescribed surface temperature field is constructed using the WOA2013 monthly climatology (Boyer et al., 2013) to which we add a small periodic in time correction to account for errors in the climatology, i.e. $\boldsymbol{\theta}_a(t) = \boldsymbol{\theta}_a^{\mathrm{WOA}}(t) + \delta\boldsymbol{\theta}_a(t)$. The unobserved correction, $\delta\boldsymbol{\theta}_a$, will be estimated as part of the Bayesian inversion. The inclusion of the $\delta\boldsymbol{\theta}_a$ term (and the $\delta\boldsymbol{s}_a$ term described below) makes this method of implementing the surface boundary condition distinctly different than the so-called "robust-diagnostic" method where the temperature is restored to the uncorrected observations (e.g. Sarmiento and Bryan, 1982).

3.3. Salinity model

For the salinity equation the source term $\boldsymbol{s}$ consists of surface freshwater fluxes, which we model by restoring the salinity in the model's upper-most layer to a seasonally varying sea surface salinity field, $\boldsymbol{s}_a(t)$, that is periodic in time, i.e. $\boldsymbol{s}_a(t + \Delta T) = \boldsymbol{s}_a(t)$. The source vector for salinity is thus given by

$$\boldsymbol{s} = \frac{1}{\tau}\mathbf{\Lambda}_s(\boldsymbol{s}_a - \mathbf{\Lambda}_s^T \boldsymbol{c}). \tag{15}$$

where $\tau = 30$ days is the restoring timescale. The prescribed sea surface salinity field is constructed using the WOA2013 (Boyer et al., 2013) monthly climatology to which we add a small periodic in time correction to account for errors in the climatology, i.e. $\boldsymbol{s}_a(t) = \boldsymbol{s}_a^{\mathrm{WOA}}(t) + \delta\boldsymbol{s}_a(t)$. The unobserved correction, $\delta\boldsymbol{s}_a$, will be estimated as part of the Bayesian inversion.

3.4. Natural radiocarbon model

For the natural (pre-bomb) radiocarbon model, the source function consists of the radioactive decay and air-sea gas exchange of $^{14}CO_2$, which we model simply as

$$\boldsymbol{s} = \frac{1}{\tau}\mathbf{\Lambda}_s({}^{14}\boldsymbol{c}_s - \mathbf{\Lambda}_s^T \boldsymbol{c}) - \lambda\boldsymbol{c}, \tag{16}$$

where $\lambda = \log(2)/(5730 \text{ years})$ is the ^{14}C decay rate, ${}^{14}\boldsymbol{c}_s$ is the GLODAP (Key et al., 2004) estimate of the surface Δ^{14}C concentration prior to the atmospheric bomb tests and $\tau = 30$ days. Because $\tau\lambda \ll 1$, we are effectively restoring $\boldsymbol{c}$ to ${}^{14}\boldsymbol{c}_s$ in the surface layer of the model.

3.5. Chlorofluorocarbons model

Chlorofluorocarbon(CFCs) are transient tracers which were released into the atmosphere starting in 1940. Therefore an initial concentration of zero is used for a transient simulation for the period from January 1940 to December 2009 using a one-month long time step. In the transient simulation, we use the atmospheric history of CFC-11 and CFC-12 (USGS, 2009) interpolated to a time resolution of one month. To model the gas exchange flux we use the standard OCMIP-2 formulation (Najjar and Orr, 1998) as was done for OCIM (DeVries, 2014),

$$\boldsymbol{s} = \frac{\boldsymbol{\Lambda}_k}{dz_1}(\boldsymbol{c}^{atm} - \boldsymbol{\Lambda}_s^T \boldsymbol{c}), \tag{17}$$

where $dz_1 = 36.1$ m is the thickness of the model's upper most layer and $\boldsymbol{c}^{atm}$ is the prescribed atmospheric CFC concentration. The gas-exchange operator $\boldsymbol{\Lambda}_k$ is an $N \times N_s$ sparse matrix with non-zero elements on the main diagonal. These are given by the piston velocity, k, scaled using an adjustable parameter α, such that

$$k = \alpha \cdot (u_{10})^2 \cdot (Sc/660)^{-\frac{1}{2}} \cdot (1 - f_{\text{ice}}), \tag{18}$$

where u_{10} is the monthly climatological root-mean-square wind speed at 10 m above the sea surface, Sc is the temperature-dependent Schmidt number, and f_{ice} is the monthly climatological fractional ice cover. Note that the scalar parameter α does not change with time and is the same in all grid boxes.

3.6. Time discretization

The version of the model we present here uses a fully implicit Euler backward time-stepping scheme with a time step of one month:

$$\begin{aligned} \mathbf{B}_n \boldsymbol{c}_n &= \boldsymbol{c}_{n-1} + \boldsymbol{s}_n^o dt, \\ \mathbf{B}_n &\equiv \mathbf{I} + \left(\boldsymbol{\Gamma}_n - \left[\frac{\partial \boldsymbol{s}}{\partial \boldsymbol{c}} \right]_n \right) dt, \end{aligned} \tag{19}$$

for $n = 1, 2, \cdots, M$ with $dt = \Delta T/12$. In this equation the time-dependent tracer transport matrix, $\boldsymbol{\Gamma}(t)$, and the partial derivative of the tracer source function with respect to the tracer concentration, $\partial \boldsymbol{s}(\boldsymbol{c}, t)/\partial \boldsymbol{c}$, are discretized into 12 time-independent matrices $\boldsymbol{\Gamma}_n$ and $[\partial \boldsymbol{s}/\partial \boldsymbol{c}]_n$ respectively for $n =$

$1, 2, \cdots, 12$, with the condition that $\mathbf{\Gamma}_{n+12} = \mathbf{\Gamma}_n$ and $[\partial \boldsymbol{s}/\partial \boldsymbol{c}]_{n+12} = [\partial \boldsymbol{s}/\partial \boldsymbol{c}]_n$. The non-homogeneous part of the source function is discretized into time-dependent source vectors, $\boldsymbol{s}(0, t_n) = \boldsymbol{s}^o_n$ for $n = 1, 2, \cdots, M$. For the transient CFC tracers we use the initial condition that $\boldsymbol{c} = 0$ and step the equations forward for $n = 1, 2, \cdots, M = N_{\rm yr} \times 12$, corresponding to the period from 1940 to 2009. For salinity, potential temperature, and pre-bomb radiocarbon the source vectors satisfy the same periodicity condition as the transport operators, i.e. $\boldsymbol{s}^o_{n+12} = \boldsymbol{s}^o_n$, implying that the fully spun-up solution ($M \to \infty$) will also be cyclo-stationary with $\boldsymbol{c}_{n+12} = \boldsymbol{c}_n$.

3.7. Cyclo-stationary solutions

With a one-month time-discretization and the Euler backward scheme the cyclo-stationary tracers (potential temperature, salinity, and pre-bomb radiocarbon) satisfy the following block-matrix system

$$\underbrace{\begin{bmatrix} -\mathbf{I}, & \mathbf{B}_1, & 0, & \cdots & 0 \\ 0 & -\mathbf{I} & \mathbf{B}_2 & \cdots & 0 \\ \vdots & & \ddots & \ddots & \vdots \\ 0 & 0 & \cdots & -\mathbf{I} & \mathbf{B}_{11} \\ \mathbf{B}_{12} & ... & ... & ... & -\mathbf{I} \end{bmatrix}}_{\tilde{\mathbf{B}}} \begin{bmatrix} \boldsymbol{c}_{12} \\ \boldsymbol{c}_1 \\ \boldsymbol{c}_2 \\ \vdots \\ \boldsymbol{c}_{11} \end{bmatrix} = \begin{bmatrix} \boldsymbol{s}^0_1 \\ \boldsymbol{s}^0_2 \\ \vdots \\ \boldsymbol{s}^0_{11} \\ \boldsymbol{s}^0_{12} \end{bmatrix} dt. \tag{20}$$

In principle one could try to obtain the cyclo-stationary solution to Eq.(20) by directly inverting $\tilde{\mathbf{B}}$, but this is computationally very expensive because of the size of $\tilde{\mathbf{B}}$. This prohibitive computational cost is particularly true if we try to decrease the size of the time-step to better resolve the seasonal cycle. We therefore solve Eq.(20) using a pre-conditioned iterative Newton-Krylov solver without explicitly constructing the $\tilde{\mathbf{B}}$ matrix or the source vector on the right hand side (e.g. Li and Primeau, 2008; Khatiwala, 2008; Bardin et al., 2014; Fu and Primeau, 2017)). In this method, we apply the preconditioner to the model state after time-stepping the model through one annual period. The preconditioner accelerates the convergence of the iterative Newton-Krylov solver, but otherwise does not affect the solution. For the preconditioner we use the same one first described in Li and Primeau (2008), namely

$$\mathbf{P} = \left(\frac{\Delta T}{12} \sum_{n=1}^{12} \left(\mathbf{\Gamma}_n - \left[\frac{\partial \boldsymbol{s}}{\partial \boldsymbol{c}} \right]_n \right) \right)^{-1} - \mathbf{I}. \tag{21}$$

It can be thought of as an approximation to equation (20) using one big Euler-backward time-step with the annually averaged tracer transport matrix. We use the `nsoli.m` Newton Krylov solver (Kelley, 2013) and obtain fully-spun up cyclo-stationary solutions with the equivalent of only a few years of simulation – typically less than 10 and seldom more than 50.

4. Bayesian inversion for the adjustable model parameters

As presently formulated the model has a suite of adjustable parameters, organized into an $980\,737 \times 1$ vector,

$$\boldsymbol{p} = \left[\begin{array}{ccccc} \partial_z \tau^{e\lambda} & \partial_z \tau^{e\phi} & \delta\boldsymbol{\theta}_a & \delta\boldsymbol{s}_a & \alpha \end{array} \right]^T, \tag{22}$$

that must be specified for the problem to be well posed. We infer the parameter values via a Bayesian inversion procedure constrained by tracer observations. Note that the parameters $\partial_z \tau^{e\lambda}$, and $\partial_z \tau^{e\phi}$ include the three-dimensional field of horizontal eddy-stress divergences as well as the correction to the imposed surface wind-stress. The two contributions cannot be separated by a our inversion procedure. The parameters $\delta\boldsymbol{\theta}_a$, and $\delta\boldsymbol{s}_a$ are the corrections to the surface temperature and salinity used to compute the fluxes of heat and freshwater at the air-sea interface. α is a scalar parameter that scales the prescribed piston velocity for the flux of CFCs through the air-sea interface.

We assign normal probability distributions to the observed tracer concentrations, with the mean of the distributions given by the model's simulated concentrations. Specifically, the probability of the tracer data conditioned on the model parameters, is given by

$$\text{prob}(\boldsymbol{c}_i^{\text{obs}} | \boldsymbol{p}) \propto \exp\left[-\frac{1}{2} (\mathbf{H}_i \boldsymbol{c}_i - \boldsymbol{c}_i^{\text{obs}})^T \mathbf{W}_i (\mathbf{H}_i \boldsymbol{c}_i - \boldsymbol{c}_i^{\text{obs}}) \right], \tag{23}$$

where the index, $i = 1, 2, \cdots 5$, identifies the particular tracer being considered, i.e. potential temperature, salinity, CFC-11, CFC-12, or pre-bomb radiocarbon. The likelihood function for potential temperature was modified from the Gaussian density by a factor that assigns a very low probability to potential temperatures that fall close to or below the freezing point of seawater, i.e. $\exp\left\{-\omega_{\text{ice}} \boldsymbol{\phi}^T \boldsymbol{\phi}\right\}$, where $\boldsymbol{\phi} = \tanh\left[\exp\left\{-(T + 2.6^\circ\text{C})/0.1^\circ\text{C}\right\}\right]$ and $\omega_{\text{ice}} = 10^4$. The matrices $\mathbf{H}_i$ are used to select the grid-boxes and months for which we have tracer observations. For potential temperature and salinity

these matrices are identity matrices because we constrain the model using the gridded climatology of WOA2013, but for the other tracers we use bottle measurements from GLODAPv2. We retained only bottle radiocarbon measurements below 1000 m for which the measured CFC-11 was less than 0.01 pmol/kg to prevent any interference with the bomb signal. The scaled precision matrices, $\mathbf{W}_i$, are taken to be the sum of two symmetric matrices one of which is positive definite. The positive definite matrix is diagonal with entries given by the reciprocals of the variances σ_i^2 computed from all the observations available for a given month and grid box (for potential temperature, salinity, and pre-bomb radiocarbon) and for a particular, grid box, month, and year for the transient CFC-11 and CFC-12 tracers, and then divided by the numbers of observations. Therefore, σ_i varies in space and time. We use the WOA13 to estimate the σ_i of temperature and salinity and GLODAPv2 to estimate the σ_i of CFCs and radiocarbon. The other matrix is given by $\beta_i \mathbf{L}^T\mathbf{L}$ where $\mathbf{L}$ is a discretized version of the horizontal Laplacian operator in spherical coordinates. The Laplacian operator is only added for the potential temperature and the salinity terms to take into account the spatially correlated errors introduced by the gridding of those observations. The value of β_i is given by one over the product of the variance of the calculated σ_i^2. We further assume that conditioned on the model, all the tracer observations are independent. With this assumption we can construct the likelihood function by simply taking the product of the probability densities for each tracer , i.e.

$$\text{prob}(\{\boldsymbol{c}_i^{\text{obs}}\}_{i=1}^{5}|\boldsymbol{p}) = \prod_{i=1}^{5} \text{prob}(\boldsymbol{c}_i^{\text{obs}}|\boldsymbol{p}). \tag{24}$$

For the prior probability of $\boldsymbol{p}$ we assume a normal distribution centered at $\boldsymbol{p} = 0$,

$$\text{prob}(\boldsymbol{p}) \propto \exp\left[-\frac{1}{2}\boldsymbol{p}^T\mathbf{W}_p\boldsymbol{p}\right], \tag{25}$$

with a prior precision matrix, $\mathbf{W}_p$, taken to be diagonal. For the unobserved errors in the wind-stress climatology, $(\delta\boldsymbol{\tau}^\lambda, \delta\boldsymbol{\tau}^\phi)$ and the unresolved eddy-stress forcing, $(\partial_z\boldsymbol{\tau}_e^\lambda, \partial_z\boldsymbol{\tau}_e^\phi)$, the diagonal of $\mathbf{W}_p$ is $\frac{1}{(0.1\mathbf{F})^2 n}$, where $\mathbf{F}$ is the forcing vector in Eq.(6), and n is the number of adjustable eddy-stress divergence parameters. This choice ensures that the large scale momentum balance follows the thermal wind and Ekman balances. (The square of $\mathbf{F}$ in this last expressions is applied element wise.) For the $\delta\boldsymbol{\theta}_a$ and $\delta\boldsymbol{s}_a$, the

diagonal elements are given by the reciprocal of the product of the variance computed from all the observation for a given month and the number of grid boxes in the surface layer of the model. We assign no prior constraint on the value of α. We further constrained the prior probability density function for the parameters implicitly by assigning a weak prior on the dynamical state of the model, i.e. we assigned a normal distribution centered at zero

$$\text{prob}(\boldsymbol{x}|\boldsymbol{p}) \propto \exp\left[-\frac{1}{2}\boldsymbol{x}^T\mathbf{W}_x\boldsymbol{x}\right], \tag{26}$$

where the precision matrix, $\mathbf{W}_x$, is taken to be diagonal. The diagonal elements are given by the reciprocal of velocity and dynamic topography variances. The horizontal velocity variances start with a value of $(1\ \text{m/s})^2$ in the top layer of the model and decay exponentially to $(0.07\ \text{m/s})^2$ at a depth of 4000 m (see Eq. 14 in Large et al., 2001). This weak constraint is helpful in the early stages of the parameter optimization as it prevents the search algorithm from suggesting parameter values that lead to implausible dynamical states. Its impact on the ultimate solution is negligible. For the vertical velocity, we increased the prior precision by a factor of 50 compared to that used by DeVries (2014), to be consistent with that used in the latest OCIM version (OCIM2), as described in (DeVries and Holzer, 2019). The increased penalty is necessary to prevent unrealistically large vertical velocities and a noisy meridional overturning circulation.

With the above choices the posterior probability density function obtained via Bayes' theorem is

$$\begin{aligned}\text{prob}(\boldsymbol{p}|\{\boldsymbol{c}_i^{\text{obs}}\}_{i=1}^5) \propto \exp\Big[&-\frac{1}{2}\sum_{i=1}^{5}(\mathbf{H}_i\boldsymbol{c}_i-\boldsymbol{c}_i^{\text{obs}})^T\mathbf{W}_i(\mathbf{H}_i\boldsymbol{c}_i-\boldsymbol{c}_i^{\text{obs}}) \\ &-\frac{1}{2}\omega_{\text{ice}}\boldsymbol{\phi}^T\boldsymbol{\phi}-\frac{1}{2}\boldsymbol{x}^T\mathbf{W}_x\boldsymbol{x}-\frac{1}{2}\boldsymbol{p}^T\mathbf{W}_p\boldsymbol{p}\Big].\end{aligned} \tag{27}$$

Note that $\boldsymbol{x}$ in this probability density is an implicit function of $\boldsymbol{p}$. The posterior probability density described by Eq. (27) lives in a 980 737 dimensional space. The large dimension of this space makes it impossible to compute or store the posterior covariance matrix of the state estimate. We therefore limit ourselves to summarizing the posterior probability density function in terms of the location of its maximum, which is equivalent to finding the minimum

of the negative logarithm of the posterior probability density function,

$$\begin{aligned}\widehat{f}(\boldsymbol{p}) \equiv & f(\boldsymbol{y}(\boldsymbol{p}), \boldsymbol{p}), \\ = & \frac{1}{2}\sum_{i=1}^{5}(\mathbf{H}_i\boldsymbol{c}_i - \boldsymbol{c}_i^{\text{obs}})^T\mathbf{W}_i(\mathbf{H}_i\boldsymbol{c}_i - \boldsymbol{c}_i^{\text{obs}}) + \frac{1}{2}\omega_{\text{ice}}\boldsymbol{\phi}^T\boldsymbol{\phi} \\ & + \frac{1}{2}\boldsymbol{x}^T\mathbf{W}_x\boldsymbol{x} + \frac{1}{2}\boldsymbol{p}^T\mathbf{W}_p\boldsymbol{p},\end{aligned} \tag{28}$$

where $\boldsymbol{y}(\boldsymbol{p}) = \left[\begin{array}{cccc}\boldsymbol{x} & \boldsymbol{c}_1 & \cdots & \boldsymbol{c}_5\end{array}\right]$ is the solution to the model equations, $F(\boldsymbol{y}, \boldsymbol{p}) = 0$, combining the cyclo-stationary dynamical state with the cyclo-stationary potential temperature, salinity and radiocarbon solutions with the transient CFC-11 and CFC-12 solutions. Note that minimizing $\widehat{f}(\boldsymbol{p})$ reduces to solving a nonlinear least-squares problem.

It is important to point out that the location of the minimum of the objective function will not change if we add a multiplicative factor to the objective function. Such a factor will, however, affect the size of the posterior error bars for our parameter estimates. Because this scaling factor affects the normalization constant for the posterior probability, introducing it also introduces an extra additive term to the objective function that depends on the scaling factor but not on $\boldsymbol{p}$. This means that if we had introduced the scaling factor we would be able to estimate its size by minimizing the resulting objective function with respect to this factor. We did not do this here because we are focusing on finding the most probable state estimate. However it will be important to estimate this missing scaling factor in the future so that we can obtain consistent posterior error bars for our state estimate.

We solve the above problem using a quasi-Newton method. Following Heinkenschloss (2008), we express the gradient of $\widehat{f}(\boldsymbol{p})$ in terms of the partial gradients of $f(\boldsymbol{y}, \boldsymbol{p})$,

$$\begin{aligned}\nabla_{\boldsymbol{p}}\widehat{f}(\boldsymbol{p}) &= \boldsymbol{y}_{\boldsymbol{p}}^T\nabla_{\boldsymbol{y}}f(\boldsymbol{y}(\boldsymbol{p}), \boldsymbol{p}) + \nabla_{\boldsymbol{p}}f(\boldsymbol{y}, \boldsymbol{p}), \\ &= -(F_{\boldsymbol{y}}(\boldsymbol{y}(\boldsymbol{p}), \boldsymbol{p})^{-1}F_{\boldsymbol{p}}(\boldsymbol{y}(\boldsymbol{p}), \boldsymbol{p}))^T\nabla_{\boldsymbol{y}}f(\boldsymbol{y}(\boldsymbol{p}), \boldsymbol{p})) + \nabla_{\boldsymbol{p}}f(\boldsymbol{y}(\boldsymbol{p}), \boldsymbol{p}), \\ &= F_{\boldsymbol{p}}(\boldsymbol{y}(\boldsymbol{p}), \boldsymbol{p})^T\boldsymbol{\lambda}(\boldsymbol{p}) + \nabla_{\boldsymbol{p}}f(\boldsymbol{y}(\boldsymbol{p}), \boldsymbol{p}),\end{aligned} \tag{29}$$

where the vector of Lagrange multipliers, $\boldsymbol{\lambda}(\boldsymbol{p})$, is the solution to

$$\left[F_{\boldsymbol{y}}(\boldsymbol{y}(\boldsymbol{p}), \boldsymbol{p})\right]^T\boldsymbol{\lambda}(\boldsymbol{p}) = -\nabla_{\boldsymbol{y}}f(\boldsymbol{y}, \boldsymbol{p}). \tag{30}$$

The great computational advantage of using the last expression in Eq. (29) rather than the middle line in Eq. (29) is that it involves solving only one linear system of equations for $\boldsymbol{\lambda}(\boldsymbol{p})$ instead of solving a separate linear system for each the 980 737 components of $\boldsymbol{p}$. Because the linear system involves the transposed Jacobian matrix, $[F_{\boldsymbol{y}}(\boldsymbol{y}(\boldsymbol{p}),\boldsymbol{p})]^T$, this method is known as the adjoint method (e.g. Schlitzer, 1993, 2007; DeVries and Primeau, 2011).

The adjoint system (30) and $\boldsymbol{\lambda(p)}$ can be partitioned into components which can be solved separately. Specifically,

$$\boldsymbol{\lambda}(\boldsymbol{p})^T = \left[\begin{array}{cccccc} \boldsymbol{\lambda}_{\boldsymbol{x}}^T & \boldsymbol{\lambda}_{\boldsymbol{\theta}}^T & \boldsymbol{\lambda}_{\boldsymbol{s}}^T & \boldsymbol{\lambda}_{\boldsymbol{c}_{14}}^T & \boldsymbol{\lambda}_{\text{CFC-11}}^T & \boldsymbol{\lambda}_{\text{CFC-12}}^T \end{array} \right] \tag{31}$$

where

$$\mathbf{B}_n^T \boldsymbol{\lambda}_{\boldsymbol{c}_n} = \boldsymbol{\lambda}_{\boldsymbol{c}_{n+1}} + \nabla_{\boldsymbol{c}_n} f(\boldsymbol{y},\boldsymbol{p}), \tag{32}$$

for $n = M, M-1, \cdots, 1$. For the cases where $\boldsymbol{c}_n$ correspond to the transient CFC tracers, the system is solved starting with the final condition $\boldsymbol{\lambda}_{\boldsymbol{c}_{M+1}} = 0$ and time-stepped backwards in time from $M = N_{\text{yr}} \times 12$ to $n = 1$. For the cyclo-stationary tracers, the $\boldsymbol{\lambda}_{\boldsymbol{c}_n}$ are also periodic and solutions are obtained using the same Newton-Krylov method used to find the cyclo-stationary state of the tracers except that the transpose of the operators are used in reverse time order, and the transpose of the operator in Eq. (21) is used for the preconditioning. We note that in the forward model, the state at time step $n+1$ is completely determined by the state of the model at time step n. Similarly, in the adjoint model, the state at time step n is completely determined by the state at time step $n+1$. Because all the solutions obtained using our cyclo-stationary solver are perfectly periodic it does not matter at which month we start the integration. We always get the same periodic solution for the same forcing.

Having obtained the Lagrange multipliers corresponding to the tracer variables, the Lagrange multipliers corresponding to the model's dynamical state can be obtained by solving for the cyclo-stationary state of

$$\mathbf{A}^T \boldsymbol{\lambda}_{\boldsymbol{x}_n} = \boldsymbol{\lambda}_{\boldsymbol{x}_{n+1}} + \mathbf{F}_n^{\dagger}, \tag{33}$$

where the monthly forcing terms are given by

$$\begin{aligned} \mathbf{F}_n^{\dagger} =& \boldsymbol{\Gamma}_{\boldsymbol{x}_n} \left[\boldsymbol{\lambda}_{\boldsymbol{\theta}_n} + \boldsymbol{\lambda}_{\boldsymbol{s}_n} + \boldsymbol{\lambda}_{\boldsymbol{c}_{14,n}} + \sum_{m=1}^{N_{\text{yr}}} \left(\boldsymbol{\lambda}_{\text{CFC-11},m,n} + \boldsymbol{\lambda}_{\text{CFC-12},m,n} \right) \right] \\ & - \nabla_{\boldsymbol{x}_n} f(\boldsymbol{y},\boldsymbol{p}), \end{aligned} \tag{34}$$

for $n = 1, 2, \cdots, 12$, where $\mathbf{\Gamma}_{\boldsymbol{x}_n}$ corresponds to the partial derivative of the tracer transport operator with respect to the dynamical state variable during month n. Cyclo-stationary solutions are obtained using the same Newton-Krylov solver used for the forward model except that the transpose of $\mathbf{A}$ is used in the preconditioner and the forcing terms are cycled in time reversed order.

4.1. Summary of CYCLOCIM data-assimilation procedure

The CYCLOCIM data-assimilation system solves the constrained optimization problem

$$\begin{aligned} &\underset{\boldsymbol{y},\boldsymbol{p}}{\text{minimize}} f(\boldsymbol{y},\boldsymbol{p}), \\ &\text{such that } C(\boldsymbol{y},\boldsymbol{p}) = 0, \end{aligned} \tag{35}$$

where $\widehat{f}(\boldsymbol{p}) = f(\boldsymbol{y}(\boldsymbol{p}),\boldsymbol{p})$ is the negative of the logarithm of the posterior probability density prob($\boldsymbol{p}|data$) for $\boldsymbol{p}$ (see Eq. 27 and Eq. 28), and $C(\boldsymbol{y},\boldsymbol{p}) = 0$ denotes the governing equations for the dynamical and tracer states of the model. The solution procedure is summarized in Figure 1. The iterative procedure consists of repeating five main steps:

1. Given a current estimate of $\boldsymbol{p}$, solve the cyclo-stationary dynamical model to obtain $\boldsymbol{x}(\boldsymbol{p})$, i.e. the seasonally varying residual mean circulation $(u^\dagger, v^\dagger, w^\dagger)$ and dynamic topography (η).
2. Solve the transient tracers ($\boldsymbol{c}_{\text{CFC-11}}$ and $\boldsymbol{c}_{\text{CFC-12}}$) and the cyclo-stationary tracers, potential temperature, salinity and natural radiocarbon ($\boldsymbol{\theta}$, $\boldsymbol{s}$, and $\boldsymbol{c}_{14}$) using the sparse-matrix tracer transport operators constructed using the current estimate of $\boldsymbol{x}$.
3. Evaluate the objective function for the given $\boldsymbol{p}$, that is, the posterior probability density function, prob($\boldsymbol{p}|data$) as given in Eq.(27). (Evaluating $\widehat{f}(\boldsymbol{p})$ as given in Eq.(28) is equivalent to evaluating Eq. (27) because the logarithm function is a monotonically increasing function.)
4. Compute the gradient of the objective function $\nabla_{\boldsymbol{p}}\widehat{f}(\boldsymbol{p})$ and check if the minimum has been reached.
5. Use a quasi-Newton search algorithm and $\nabla_{\boldsymbol{p}}\widehat{f}(\boldsymbol{p})$ to produce an improved (more probable) estimate of $\boldsymbol{p}$.

The data assimilation procedure we use is equivalent to what is sometimes called a 4-D variational assimilation system except that the time-dependent part of the procedure is restricted to be periodic for the circulation and the non-transient tracers.

5. Results

We conducted state estimates for a version of CYCLOCIM with a resolution of $8^\circ \times 8^\circ \times 22$ layers and $4^\circ \times 4^\circ \times 24$ layers. The optimization for a version of CYCLOCIM with the standard OCIM resolution of $2^\circ \times 2^\circ \times 24$ layers is underway, but the optimal solution has not yet been found. We stop the iteration when the cost function changes by less than 1% per 1,000 iteration. Note that for the $8^\circ \times 8^\circ$ and $4^\circ \times 4^\circ$ versions of CYCLOCIM we prescribed a maximum number of iterations but we checked that the above stopping criteria was met for the solutions we present here. Our goal is to present the higher resolution solution in a separate paper that can focus on the state estimate rather than the technical aspects of the assimilation, which is the main focus of the present report.

The evolution of the objective function for the $8^\circ \times 8^\circ \times 22$ model for the 10 000 iterations is shown in Figure 2. The objective function starts at a value of approximately 10^4. After 10,000 iterations the objective function has decreased to a value of less than 5.4. The drop is fastest for the first 2000 iterations and the rate of decrease slows down afterwards. While the rate of decrease is modest in the last 1000 iterations, $\widehat{f}(\boldsymbol{p})$ is still decreasing monotonically. However the changes in the resulting state estimate are rather modest. For the version of CYCLOCIM with a $4^\circ \times 4^\circ \times 24$ layers resolution, which we present in the next section, we performed approximately 4×10^3 iterations but we restarted the optimization along the way because we did not include all the tracer constraints at the beginning.

The magnitude of the estimated eddy-stress divergence terms, which also includes effects due to the missing nonlinear terms and discretization errors, is comparable to the magnitude of the error terms from the original steady state OCIM model (DeVries and Primeau, 2011). The horizontally averaged magnitude of the vertical divergence of the eddy stresses is $\sim 1.2\times10^{-6}$ m/s^2. The magnitude of these parameterized forcing terms are only modestly dependent on the model resolution (i.e. $8^\circ \times 8^\circ$, $4^\circ \times 4^\circ$, or $2^\circ \times 2^\circ$). For comparison the explicit forcing appearing on the right hand side of the horizontal momentum equation has a typical horizontally averaged magnitude that is about of factor of three bigger. This suggests that the non-parameterized large-scale momentum balance dominates over the parameterized eddy-stresses, and confirms that the relative weights we have assigned to the likelihood and prior in our probability model provide an acceptable initial estimate. Further refinements might be necessary if the goal is to interpret the resulting

eddy-stress terms physically.

5.1. Comparison of assimilated variables with observations

We begin by comparing each modeled tracer with the observations that were used to constrain the model. In Figures 3 - 7, we perform the comparison on the model's $4^\circ \times 4^\circ$ grid. It is therefore important to keep in mind that any variance in the data associated with sharp gradients that cannot be resolved by this coarse mesh will necessarily be ignored in the comparison.

A summary of the model fit to the data is provided in Figure 3 where we show the joint cumulative distribution functions for the observed and modeled tracer variables. For all tracers, more than 90% of the ocean volume has concentrations that cluster tightly along the 1:1 line with $R^2 = 0.99$ for potential temperature, and $R^2 \approx 0.96$ for the other tracers. The close agreement between the modelled and observed tracers suggests that the CYCLOCIM circulation can be used to produce meaningful estimates of the climatological water mass formation rates and transport for the real ocean, which is not always possible when analyzing free-running prognostic models.

In Figure 4 the globally averaged root mean square errors (RMSE) for the potential temperature, salinity and CFC-11 from CYCLOCIM are compared to the corresponding RMSEs for the OCIM CTRL state estimate (DeVries, 2014). By resolving the seasonal cycle, CYCLOCIM provides a better fit to the observations at mid to high latitudes in the surface mixed layer and seasonal thermocline. For the deep ocean below 500 m, where seasonality is negligible, the RMSE is similar for both state estimates.

The globally averaged RMSE of potential temperature for CYCLOCIM is 0.29°C, whereas for OCIM it is 0.38°C. For the near-surface waters, 0 – 200m, the decrease in the RMSE is significantly larger: 0.70°C for CYCLOCIM versus 1.27°C for OCIM. Most of the improvements occur in mid-latitudes (Figure 5) where the mixed layer depths have a pronounced seasonal variation. For example, the cold bias of more than 3°C to the North of the Kuroshio Extension in the OCIM state estimate is substantially decreased in the CYCLOCIM state estimate. Similarly, the low-latitude warm bias in the OCIM state estimate has been eliminated in the CYCLOCIM state estimate. Consistent with the results of Yu and Malanotte-Rizzoli (1998), resolving the seasonal variations produces a significantly improved estimate of the climatological circulation.

The ability of the model to capture the correct seasonal cycle is illustrated in Figure 6 in which we compare the potential temperature anomalies

(plotted as departure from the annual average) along 36°S for CYCLOCIM and the WOA2013 observations (Boyer et al., 2013). The modeled potential temperature shows a similar seasonal pattern as the observations. In the summer (DJF), the mixed layer is shallow and there is a strong temperature gradient near the surface. The mixed layer deepens through the fall (MAM) and winter (JJA), becoming thickest in late winter when the surface stratification entirely disappears. In spring (SON), as winds weaken and solar irradiance increases, the mixed layer shoals once again. The model seasonality is quite similar to that of the observations. Exceptions are along the western boundary currents where the warm and cold anomalies penetrate deeper in the observations than in the model. Such errors are not surprising given the coarseness of the model resolution. We anticipate that these errors will be reduced in the $2^\circ \times 2^\circ$-CYCLOCIM and by including the dynamic topography constraints from satellite altimeter data.

There are also significant improvements in the CYCLOCIM-simulated surface salinity fields as can be seen from Figure 7 where we plot the errors averaged over the top 200 m of the water column. Most prominently, large errors in the western part of the subpolar gyre in the North Atlantic ocean present in the steady OCIM state estimate are greatly reduced in the seasonally varying CYCLOCIM state estimate. A similar positive bias in the Southern Ocean for the steady OCIM state estimate has been completely eliminated in the CYCLOCIM state estimate. Improvements extend over most of the ocean with the exception of the Arctic basin where a uniformly positive salinity bias in OCIM has been replaced by errors that appear more random. The globally averaged RMSE for salinity in the upper 200 m of the water column is reduced from 0.25 g/kg for OCIM to 0.11 g/kg for CYCLOCIM. For the full water column, the improvements are more modest but still appreciable with RMSE reduced from 0.07 g/kg for OCIM to 0.04 g/kg for CYCLOCIM.

The CYCLOCIM simulation of CFC-11 also provides a better fit to the observed CFC-11 data. (The sensitivity of the fit to the scaling parameter for the piston velocity is discussed in Appendx A.3). The RMSE for surface waters between 0 and 200m is 0.07 pmol/kg for the OCIM state estimate whereas for CYCLOCIM it is 0.04 pmol/kg. In Figure 8 we plot the decadal-mean zonal averages of CFC-11 and CFC-12 concentrations. The zonal averages are calculated using a volume weighted average of the CFC concentrations for gridboxes with at least one CFC measurement at any depth and longitude during the particular decade. The agreement between

CYCLOCIM and the observations is generally good. There are however clear decadal biases at high latitudes in the Southern Ocean. South of 60°S the model concentrations are several standard deviations too low for the 1980-1989 and the 2000-2009 period while being in very good agreement for the 1990-1999 period. In the North there are similar low biases but the exact latitude band with the largest biases appear to shift from decade to decade. Decadal variability in the ventilation of the ocean provides a plausible explanation for these errors (e.g. Waugh et al., 2013; DeVries et al., 2017).

The CYCLOCIM fit to the pre-bomb radiocarbon is also very good. Figure 9 compares the zonally-averaged CYCLOCIM simulated radiocarbon to the GLODAPv2 data (Olsen et al., 2016). The zonal averages are calculated using a volume weighted average using only grid-boxes below 1000 m with CFC-11 concentrations below 0.01 pmol/kg.The good agreement between CYCLOCIM and the GLODAPv2 radiocarbon at all latitudes and in all basins suggests that the deep-ocean ventilation timescales in CYCLOCIM are comparable to those of the real ocean.

5.2. Meridional overturning circulation

The climatological mean meridional overturning circulation (MOC) is defined as the stream function for the zonally integrated meridional volume transport with depth. Figure 10(a)-(c) shows the implied stream function for CYCLOCIM in the Southern Ocean, Pacific Ocean and Atlantic Ocean. The estimated overturning circulation appears consistent with typical results from inverse models (Lumpkin and Speer, 2007; DeVries and Primeau, 2011; DeVries and Holzer, 2019; Cessi, 2019). The maximum of the stream function is approximately -30 Sv in the Southern Ocean ($\sim$ 60 °S), 22 Sv in the Northern Atlantic, and -8 Sv across the equator in the deep Pacific Ocean.

5.3. Inferred air-sea fluxes and meridional transport of heat and freshwater

In contrast to the OCIM state estimate, we did not use the heat and freshwater reanalysis fluxes to constrain the CYCLOCIM state estimate. It is therefore interesting to examine how the inferred meridional heat and freshwater transports compare to other data-based estimates.

Figure 11 shows the seasonally averaged surface heat flux. During June to August the ocean gains heat in the northern hemisphere and loses it in the southern hemisphere, while the reverse is true in the December to February months. The shoulder seasons (March-May and September-November) have

more muted air-sea heat flux patterns with the ocean generally gaining heat at low latitudes and losing heat at high latitudes.

In Figure 12(a) we show the annually-average CYCLOCIM estimate of the air-sea heat flux. The ocean gains heat in the East Pacific cold tongue region and along the eastern boundaries of the Pacific and Atlantic with magnitude around 150 Wm^{-2}. Heat gained in the tropical regions is transported poleward and is lost in higher latitudes. In Figure 12(b) we compare the mean meridional transport computed from the CYCLOCIM state estimate to estimates from the CORE.v2 reanalysis (Large and Yeager, 2009), from OCIM-CTRL (DeVries, 2014) and from a not-fully-converged estimate using a version of CYCLOCIM with a horizontal resolution of $2^\circ \times 2^\circ$ (CYLCOCIM2x2). Before discussing these results we hesitate to point out that as presently configured the model shows great sensitivity to the choice of restoring timescale τ used in the surface boundary condition for heat and freshwater (See Appendix A.2). The CYCLOCIM meridional heat transport peaks near 20°N with a value of 2 PW and near 20°S with a value of 1 PW. The meridional heat transports for CYCLOCIM2x2 and OCIM also peak near 20°N but with weaker values of 1.2, 1.5 PW respectively, and at 15°S with a consistent value of approximately 1 PW. In the southern hemisphere there is a general agreement between OCIM, CYCLOCIM and CYCLOCIM2x2, which in turn predict a significantly larger poleward heat transport than CORE.v2. The larger poleward heat transport in southern hemisphere is also consistent with the ECCO estimate (Forget and Ferreira, 2019) and from the atmospheric reanalyses (Trenberth and Fasullo, 2017). In the northern hemisphere south of $\sim 50^\circ$N the CORE.v2 meridional heat transport tends to be smaller than that of CYCLOCIM but larger than that of OCIM and CYCLOCIM2x2. Northward of $\sim 50^\circ$N CYCLOCIM predicts a significantly smaller poleward heat transport than either CORE.v2, OCIM, CYCLOCIM2x2. The air-sea heat fluxes in the Kuroshio and Gulf Stream regions for the CYCLOCIM state estimate are substantially weaker than those for the CORE.v2 reanalysis (not shown). The annually averaged heat loss to the atmosphere in the Gulf Stream region as estimated from CYCLOCIM is around 50 Wm^{-2}, while in the Labrador Sea the annually averaged heat loss is greater than 300 Wm^{-2}. Such a large heat loss to the atmosphere would suggest a large meridional heat transport to the north of 50°N, yet the CYCLOCIM estimate appears to be substantially weaker than either the CORE.v2, OCIM, or CYLCOCIM2x2 estimates. This apparent inconsistency can be explained by the fact that CYCLCOCIM produces an

unrealistic southward heat transport near 50°N in the Pacific basin, which more than compensates for the unrealistically large northward heat transport in the Atlantic basin. The CYLCOCIM2x2 estimate does not appear to produce the unrealistic southward heat transport in the Pacific basin, which is encouraging, but it does point to the sensitivity of the inferred pattern of air-sea heat fluxes to the horizontal resolution of the model in addition to a strong sensitivity to the choice of restoring time-scale used in the surface boundary condition for temperature and salinity.

The implied annually averaged freshwater fluxes (Figure 12(c)) shows a pattern that is similar to the CORE.v2 reanalysis data (not shown) (Large and Yeager, 2009). There is net evaporation in the subtropical gyres and net precipitation in the intertropical convergence zone (ITCZ) and the sub-polar regions. However, CYCLOCIM predicts weak precipitation minus evaporation in the ITCZ with a magnitude around 1 m/year and strong precipitation minus evaporation in the Gulf Stream region and Labrador Sea with magnitude more than 3 m/year. In the COREv2 reanalysis, there is 1.5 m/year of precipitation minus evaporation in the ITCZ, and 1 m/year of precipitation minus evaporation in the Gulf Stream region and Labrador Sea. Figure 12(d) compares the meridional freshwater transport estimate from CYCLOCIM, CYCLOCIM2x2 to those of CORE.v2 and OCIM. The largest disagreement is in the northern hemisphere between the equator and $\sim$ 40°N where CYCLOCIM predicts a strong southward freshwater transport whereas both OCIM and the CORE.v2 estimates show a northward transport between $\sim$ 5°N and 20°N and a substantially weaker southward transport than CYCLOCIM between 20°N and 40° N. The CYCLOCIM2x2 estimate is generally closer to the OCIM and CORE.v2 estimates implying again that the surface flux patterns are quite sensitive to the horizontal resolution of the model.

The differences between the CORE.v2 reanalysis and the CYCLOCIM inferred meridional heat and freshwater transport suggest that in future inversions we might obtain improved state estimates by including atmospheric reanalysis constraints in the probability model as we did previously for OCIM. On the other hand CYCLOCIM2x2 produces reasonable first-order estimate of the meridional transports of heat and freshwater that are independent of atmospheric reanalyses. Without a more thorough uncertainty analysis it is difficult to unequivocally select one estimate over another as being more representative of the true climatological meridional transports. Such an uncertainty analysis is planned for the $2^\circ \times 2^\circ$ version of CYCLOCIM.

6. Summary and discussion

We have presented the formulation of a 4-D variational assimilation system for estimating the climatological mean seasonal cycle of the residual-mean ocean circulation. The system, which we call CYCLOCIM, assimilates monthly mean potential temperature and salinity data from the WOA2013, transient CFC-11 and CFC-12 data from the GLODAPv2 database, and natural radiocarbon measurements for the deep ocean from the GLODAPv2 database.

We have demonstrated that our data-constrained model produces a plausible overturning circulation. While the meridional heat and freshwater transports are quite sensitive to the model's horizontal resolution, the $2^\circ \times 2^\circ$ version of CYCLOCIM produces estimates that are in rough agreement with existing estimates even though the objective function did not explicitly include such constraints. By resolving the seasonal cycle we are able to produce a much better fit to observations in the upper ocean compared to our previous steady-state OCIM estimates, and most of the assimilated variables are in agreement with the observational constraints. One exception is the CFC-11 and CFC-12 tracers in the Antarctic region of the Southern Ocean, where CYCLOCIM concenrations are too low. Decadal variability in the ventilation of the ocean provides a plausible explanation for these errors (e.g. Waugh et al., 2013; DeVries et al., 2017).

The main product of our assimilation system is a set of 12 monthly data-constrained tracer transport operators for the climatological annual cycle of the ocean circulation. We anticipate that these operators will be particularly useful for global biogeochemical inversions for which there is a need for reliable estimates of the seasonally varying climatological transport of tracers. We focused on the estimate produced using CYCLOCIM with a $4^\circ \times 4^\circ$ resolution, but we are presently completing the optimization for the $2^\circ \times 2^\circ$ version of the model. For expediency we also ignored valuable constraints on the dynamic topography of the model provided by satellite altimeter data. We plan on including this constraint in future versions of CYCLOCIM. Another avenue for future work is to produce an ensemble of tracer transport operators drawn from the Bayesian posterior distribution for the eddy-stresses and surface forcing. So far we have only determined the maximum of the posterior distribution but the development of a computationally efficient means of drawing samples from the posterior should be a high priority for future work, so that realistic error estimates can be provided.

In principle, CYCLOCIM could also be used to estimate the eddy-stresses as was done in the work of Ferreira et al. (2005). However, as presently formulated the tracer transport errors due to the coarse space and time resolution of the model get partially corrected via adjustments of the eddy-stress terms. This makes the eddy-stress terms noisy and difficult to interpret. It might also be necessary to replace the Rayleigh drag in the momentum equation with a laplacian viscosity as was done in the original OCIM (DeVries and Primeau, 2011) but subsequently replaced with the computationally more efficient from Rayleigh drag (DeVries, 2014). For our present goal of generating high fidelity tracer transport operators our inability to separate physical eddy-stress from noise is not a major problem, but if the goal is to study the eddy-stresses it will be important to separate these two contributions to the eddy-stress control variables in the model.

7. Acknowledgments

QH and FP acknowledge support from National Science Foundation Grant 1658380. TD acknowledges support from NSF award OCE-1658392.

References

Balmaseda, M.A., Hernandez, F., Storto, A., Palmer, M.D., Alves, O., Shi, L., Smith, G.C., Toyoda, T., Valdivieso, M., Barnier, B., Behringer, D., Boyer, T., Chang, Y.S., Chepurin, G.A., Ferry, N., Forget, G., Fujii, Y., Good, S., Guinehut, S., Haines, K., Ishikawa, Y., Keeley, S., Köhl, A., Lee, T., Martin, M.J., Masina, S., Masuda, S., Meyssignac, B., Mogensen, K., Parent, L., Peterson, K.A., Tang, Y.M., Yin, Y., Vernieres, G., Wang, X., Waters, J., Wedd, R., Wang, O., Xue, Y., Chevallier, M., Lemieux, J.F., Dupont, F., Kuragano, T., Kamachi, M., Awaji, T., Caltabiano, A., Wilmer-Becker, K., Gaillard, F., 2015. The Ocean Reanalyses Intercomparison Project (ORA-IP). Journal of Operational Oceanography 8, s80–s97. URL: https://doi.org/10.1080/1755876X.2015.1022329, doi:10.1080/1755876X.2015.1022329.

Bardin, A., Primeau, F., Lindsay, K., 2014. An offline implicit solver for simulating prebomb radiocarbon. Ocean Modelling 73, 45–58. URL: http://dx.doi.org/10.1016/j.ocemod.2013.09.008, doi:10.1016/j.ocemod.2013.09.008.

Botev, Z.I., Grotowski, J.F., Kroese, D.P., 2010. Kernel density estimation via diffusion. Ann. Statist. 38, 2916–2957. URL: https://doi.org/10.1214/10-AOS799, doi:10.1214/10-AOS799.

Boyer, T.P., Antonov, J.I., Baranova, O.K., Garcia, H.E., Johnson, D.R., Mishonov, A.V., O'Brien, T.D., Seidov 1948-, D., Smolyar, I.I., Zweng, M.M., Paver, C.R., Locarnini, R.A., Reagan, J.R., Forgy, C.C., Grodsky, A., Levitus, S., 2013. World ocean database 2013. URL: https://repository.library.noaa.gov/view/noaa/1291, doi:http://doi.org/10.7289/V5NZ85MT.

Brix, H., Menemenlis, D., Hill, C., Dutkiewicz, S., Jahn, O., Wang, D., Bowman, K., Zhang, H., 2015. Using green's functions to initialize and adjust a global, eddying ocean biogeochemistry general circulation model. Ocean Modelling 95, 1 – 14. URL: http://www.sciencedirect.com/science/article/pii/S1463500315001171, doi:https://doi.org/10.1016/j.ocemod.2015.07.008.

Carroll, D., Menemenlis, D., Adkins, J.F., Bowman, K.W., Brix, H., Dutkiewicz, S., Fenty, I., Gierach, M.M., Hill, C., Jahn, O., Landschützer,

P., Lauderdale, J.M., Liu, J., Manizza, M., Naviaux, J.D., Rödenbeck, C., Schimel, D.S., Van der Stocken, T., Zhang, H., 2020. The ecco-darwin data-assimilative global ocean biogeochemistry model: Estimates of seasonal to multi-decadal surface ocean pco2 and air-sea co2 flux. Journal of Advances in Modeling Earth Systems n/a, e2019MS001888. URL: https://agupubs.onlinelibrary.wiley.com/doi/abs/10.1029/2019MS001888, doi:10.1029/2019MS001888, arXiv:https://agupubs.onlinelibrary.wiley.com/doi/pdf/10 e2019MS001888 2019MS001888.

Cessi, P., 2019. The global overturning circulation. Annual Reviews, Palo Alto. volume 11 of *Annual Review of Marine Science*. pp. 249–270. doi:10.1146/annurev-marine-010318-095241.

de Boyer Montégut, C., Madec, G., Fischer, A.S., Lazar, A., Iudicone, D., 2004. Mixed layer depth over the global ocean: An examination of profile data and a profile-based climatology. Journal of Geophysical Research: Oceans 109. URL: https://doi.org/10.1029/2004JC002378, doi:10.1029/2004JC002378.

DeVries, T., 2014. The oceanic anthropogenic CO2 sink: Storage, air-sea fluxes, and transports over the industrial era. Global Biogeochemical Cycles 28, 631–647. URL: https://agupubs.onlinelibrary.wiley.com/doi/abs/10.1002/2013GB004739, doi:10.1002/2013GB004739.

Devries, T., Deutsch, C., 2014. Large-scale variations in the stoichiometry of marine organic matter respiration. Nature Geoscience 7, 890–894. doi:10.1038/ngeo2300.

DeVries, T., Deutsch, C., Rafter, P.A., Primeau, F., 2013. Marine denitrification rates determined from a global 3-D inverse model. Biogeosciences 10, 2481–2496. doi:10.5194/bg-10-2481-2013.

DeVries, T., Holzer, M., 2019. Radiocarbon and Helium Isotope Constraints on Deep Ocean Ventilation and Mantle-3He Sources. Journal of Geophysical Research: Oceans 124, 3036–3057. URL: https://agupubs.onlinelibrary.wiley.com/doi/abs/10.1029/2018JC014716, doi:10.1029/2018JC014716.

DeVries, T., Holzer, M., Primeau, F., 2017. Recent increase in oceanic carbon uptake driven by weaker upper-ocean overturning. Nature 542, 215–218. URL: http://dx.doi.org/10.1038/nature21068, doi:10.1038/nature21068.

DeVries, T., Primeau, F., 2011. Dynamically and Observationally Constrained Estimates of Water-Mass Distributions and Ages in the Global Ocean. Journal of Physical Oceanography 41, 2381–2401. URL: http://journals.ametsoc.org/doi/abs/10.1175/JPO-D-10-05011.1, doi:10.1175/JPO-D-10-05011.1.

Devries, T., Primeau, F., Deutsch, C., 2012. The sequestration efficiency of the biological pump. Geophysical Research Letters 39, 1–5. doi:10.1029/2012GL051963.

Doi, T., Osafune, S., Sugiura, N., Kouketsu, S., Murata, A., Masuda, S., Toyoda, T., 2015. Multidecadal change in the dissolved inorganic carbon in a long-term ocean state estimation. Journal of Advances in Modeling Earth Systems 7, 1885–1900. URL: https://agupubs.onlinelibrary.wiley.com/doi/abs/10.1002/2015MS000462, doi:10.1002/2015MS000462, arXiv:https://agupubs.onlinelibrary.wiley.com/doi/pdf/10

Ferreira, D., Marshall, J., Heimbach, P., 2005. Estimating Eddy Stresses by Fitting Dynamics to Observations Using a Residual-Mean Ocean Circulation Model and Its Adjoint. Journal of Physical Oceanography 35, 1891–1910. URL: ttps://doi.org/10.1175/JPO2785.1, doi:10.1175/JPO2785.1.

Forget, G., Campin, J.M., Heimbach, P., Hill, C.N., Ponte, R.M., Wunsch, C., 2015. ECCO version 4: an integrated framework for non-linear inverse modeling and global ocean state estimation. Geoscientific Model Development 8, 3071–3104. doi:10.5194/gmd-8-3071-2015.

Forget, G., Ferreira, D., 2019. Global ocean heat transport dominated by heat export from the tropical pacific. Nature Geoscience 12.

Frants, M., Holzer, M., DeVries, T., Matear, R., 2015. Constraints on the global marine iron cycle from a simple inverse model. Journal of Geophysical Research: Biogeosciences 121, 28–51. URL:

https://agupubs.onlinelibrary.wiley.com/doi/abs/10.1002/2015JG003111, doi:10.1002/2015JG003111.

Fu, W., Primeau, F., 2017. Application of a fast Newton–Krylov solver for equilibrium simulations of phosphorus and oxygen. Ocean Modelling 119, 35–44. URL: https://doi.org/10.1016/j.ocemod.2017.09.005, doi:10.1016/j.ocemod.2017.09.005.

Fukumori, I., Heimbach, P., Ponte, R.M., Wunsch, C., 2018. A Dynamically Consistent, Multivariable Ocean Climatology. Bulletin of the American Meteorological Society 99, 2107–2128. URL: https://doi.org/10.1175/BAMS-D-17-0213.1, doi:10.1175/BAMS-D-17-0213.1, arXiv:https://journals.ametsoc.org/bams/article-pdf/99/10/2107/3748788/

Ganachaud, A., Wunsch, C., 2000. Improved estimates of global ocean circulation, heat transport and mixing from hydrographic data. Nature 408, 453–457. URL: https://doi.org/10.1038/35044048, doi:10.1038/35044048.

Ghil, M., Malanotte-Rizzoli, P., 1991. Data assimilation in meteorology and oceanography. Advances in geophysics 33, 141–266. doi:10.1016/S0065-2687(08)60442-2.

Graven, H.D., Gruber, N., Key, R., Khatiwala, S., Giraud, X., 2012. Changing controls on oceanic radiocarbon: New insights on shallow-to-deep ocean exchange and anthropogenic co2 uptake. Journal of Geophysical Research: Oceans 117. URL: https://agupubs.onlinelibrary.wiley.com/doi/abs/10.1029/2012JC008074, doi:10.1029/2012JC008074, arXiv:https://agupubs.onlinelibrary.wiley.com/doi/pdf/10.

Haltiner, G.J., Williams, R.T., 1980. Numerical Prediction and Dynamical Meteorology Second Edition. John Wiley & Sons.

Heinkenschloss, M., 2008. Numerical solution of implicitly constrained optimization problems. CAAM Technical Report .

Holzer, M., DeVries, T., Bianchi, D., Newton, R., Schlosser, P., Winckler, G., 2017. Objective estimates of mantle ^{3}He in the ocean and implications for constraining the deep ocean

circulation. Earth and Planetary Science Letters 458, 305–314. URL: http://dx.doi.org/10.1016/j.epsl.2016.10.054, doi:10.1016/j.epsl.2016.10.054.

Holzer, M., Frants, M., Pasquier, B., 2016. The age of iron and iron source attribution in the ocean. Global Biogeochemical Cycles 30, 1454–1474. doi:10.1002/2016GB005418.

Holzer, M., Primeau, F.W., 2013. Global teleconnections in the oceanic phosphorus cycle: Patterns, paths, and timescales. Journal of Geophysical Research: Oceans 118, 1775–1796. doi:10.1002/jgrc.20072.

Holzer, M., Primeau, F.W., DeVries, T., Matear, R., 2014. The Southern Ocean silicon trap: Data-constrained estimates of regenerated silicic acid, trapping efficiencies, and global transport paths. Journal of Geophysical Research: Oceans 119, 313–331. doi:10.1002/2013JC009356.

John, S.G., Helgoe, J., Townsend, E., Weber, T., DeVries, T., Tagliabue, A., Moore, K., Lam, P., Marsay, C.M., Till, C., 2018. Biogeochemical cycling of Fe and Fe stable isotopes in the Eastern Tropical South Pacific. Marine Chemistry 201, 66–76. URL: http://dx.doi.org/10.1016/j.marchem.2017.06.003, doi:10.1016/j.marchem.2017.06.003.

Kelley, C.T., 2013. Solving nonlinear equations with Newton's method. Society for Industrial and Applied Mathematics, Philadelphia, PA.

Key, R.M., Kozyr, A., Sabine, C.L., Lee, K., Wanninkhof, R., Bullister, J.L., Feely, R.A., Millero, F.J., Mordy, C., Peng, T.H., 2004. A global ocean carbon climatology: Results from global data analysis project (glodap). Global Biogeochemical Cycles 18. URL: https://agupubs.onlinelibrary.wiley.com/doi/abs/10.1029/2004GB002247, doi:10.1029/2004GB002247.

Khatiwala, S., 2008. Fast spin up of Ocean biogeochemical models using matrix-free Newton-Krylov. Ocean Modelling 23, 121–129. doi:10.1016/j.ocemod.2008.05.002.

Köhl, A., 2015. Evaluation of the gecco2 ocean synthesis: transports of volume, heat and freshwater in the atlantic. Quarterly

Journal of the Royal Meteorological Society 141, 166–181. URL: https://rmets.onlinelibrary.wiley.com/doi/abs/10.1002/qj.2347, doi:10.1002/qj.2347, arXiv:https://rmets.onlinelibrary.wiley.com/doi/pdf/10.1002/qj

Large, W.G., Danabasoglu, G., McWilliams, J.C., Gent, P.R., Bryan, F.O., 2001. Equatorial Circulation of a Global Ocean Climate Model with Anisotropic Horizontal Viscosity. Journal of Physical Oceanography 31, 518–536. URL: https://doi.org/10.1175/1520-0485(2001)031<0518:ECOAGO>2.0.CO;2, doi:10.1175/1520-0485(2001)031¡0518:ECOAGO¿2.0.CO;2, arXiv:https://journals.ametsoc.org/jpo/article-pdf/31/2/518/4446943/1520-0485(20

Large, W.G., Yeager, S.G., 2009. The global climatology of an interannually varying air–sea flux data set. Climate Dynamics 33, 341–364. URL: https://doi.org/10.1007/s00382-008-0441-3, doi:10.1007/s00382-008-0441-3.

Leonard, B.P., 1979. A stable and accurate convective modelling procedure based on quadratic upstream interpolation. Computer Methods in Applied Mechanics and Engineering 19, 59–98. URL: http://www.sciencedirect.com/science/article/pii/0045782579900343, doi:https://doi.org/10.1016/0045-7825(79)90034-3.

Li, X., Primeau, F.W., 2008. A fast Newton-Krylov solver for seasonally varying global ocean biogeochemistry models. Ocean Modelling 23, 13–20. doi:10.1016/j.ocemod.2008.03.001.

Liu, C., Köhl, A., Stammer, D., 2012. Adjoint-Based Estimation of Eddy-Induced Tracer Mixing Parameters in the Global Ocean. Journal of Physical Oceanography 42, 1186–1206. URL: https://doi.org/10.1175/JPO-D-11-0162.1, doi:10.1175/JPO-D-11-0162.1.

Lumpkin, R., Speer, K., 2007. Global Ocean Meridional Overturning. Journal of Physical Oceanography 37, 2550–2562. doi:10.1175/JPO3130.1.

Marshall, J., Schott, F., 1999. Open-ocean convection: Observations, theory, and models. Reviews of Geophysics 37, 1–64. URL: https://agupubs.onlinelibrary.wiley.com/doi/abs/10.1029/98RG02739, doi:10.1029/98RG02739.

Martin, T.S., Primeau, F., Casciotti, K.L., 2019a. Assessing marine nitrogen cycle rates and process sensitivities with a global 3-d inverse model. Global Biogeochemical Cycles 33, 1026–1047. URL: https://agupubs.onlinelibrary.wiley.com/doi/abs/10.1029/2018GB006088, doi:10.1029/2018GB006088, arXiv:https://agupubs.onlinelibrary.wiley.com/doi/pdf/10

Martin, T.S., Primeau, F., Casciotti, K.L., 2019b. Assessing marine nitrogen cycle rates and process sensitivities with a global 3D inverse model. Global Biogeochem. Cycles accepted August 4, n.a.

Mazloff, M.R., Heimbach, P., Wunsch, C., 2010. An Eddy-Permitting Southern Ocean State Estimate. Journal of Physical Oceanography 40, 880–899. URL: https://doi.org/10.1175/2009JPO4236.1, doi:10.1175/2009JPO4236.1, arXiv:https://journals.ametsoc.org/jpo/article-pdf/40/5/

Najjar, R.G., Orr, J., 1998. Design of ocmip-2 simulations of chlorofluorocarbons , the solubility pump and common biogeochemistry. URL: http://www.cgd.ucar.edu/oce/OCMIP/design.pdf.

Olsen, A., Key, R.M., van Heuven, S., Lauvset, S.K., Velo, A., Lin, X., Schirnick, C., Kozyr, A., Tanhua, T., Hoppema, M., Jutterström, S., Steinfeldt, R., Jeansson, E., Ishii, M., Pérez, F.F., Suzuki, T., 2016. The global ocean data analysis project version 2 (glodapv2) – an internally consistent data product for the world ocean. Earth System Science Data 8, 297–323. URL: https://www.earth-syst-sci-data.net/8/297/2016/, doi:10.5194/essd-8-297-2016.

Osafune, S., Masuda, S., Sugiura, N., Doi, T., 2015. Evaluation of the applicability of the estimated state of the global ocean for climate research (estoc) data set. Geophysical Research Letters 42, 4903–4911. URL: https://agupubs.onlinelibrary.wiley.com/doi/abs/10.1002/2015GL064538, doi:10.1002/2015GL064538, arXiv:https://agupubs.onlinelibrary.wiley.com/doi/pdf/10

Pasquier, B., Holzer, M., 2016. The plumbing of the global biological pump: Efficiency control through leaks, pathways, and time scales. Journal of Geophysical Research: Oceans 121, 6367–6388. doi:10.1002/2016JC011821.

Pasquier, B., Holzer, M., 2017. Inverse-model estimates of the ocean's coupled phosphorus, silicon, and iron cycles. Biogeosciences 14, 4125–4159. doi:10.5194/bg-14-4125-2017.

Primeau, F.W., Holzer, M., DeVries, T., 2013. Southern Ocean nutrient trapping and the efficiency of the biological pump. Journal of Geophysical Research: Oceans 118, 2547–2564. doi:10.1002/jgrc.20181.

Roshan, S., DeVries, T., 2017. Efficient dissolved organic carbon production and export in the oligotrophic ocean. Nature Communications 8, 2036. URL: http://www.nature.com/articles/s41467-017-02227-3, doi:10.1038/s41467-017-02227-3.

Roshan, S., Wu, J., DeVries, T., 2017. Controls on the Cadmium-Phosphate Relationship in the Tropical South Pacific. Global Biogeochemical Cycles 31, 1516–1527. doi:10.1002/2016GB005556.

Sarmiento, J.L., Bryan, K., 1982. An ocean transport model for the North Atlantic. Journal of Geophysical Research: Oceans 87, 394–408. URL: https://agupubs.onlinelibrary.wiley.com/doi/abs/10.1029/JC087iC01p00394, doi:10.1029/JC087iC01p00394.

Schlitzer, R., 1993. Determining the mean, large-scale circulation of the Atlantic with the adjoint method. Journal of Physical Oceanography 23, 1935–1952.

Schlitzer, R., 2007. Assimilation of Radiocarbon and Chlorofluorocarbon Data to Constrain Deep and Bottom Water Transports in the World Ocean. Journal of Physical Oceanography 37, 259–276. URL: http://journals.ametsoc.org/doi/abs/10.1175/JPO3011.1, doi:10.1175/JPO3011.1.

Stammer, D., Ueyoshi, K., Köhl, A., Large, W.G., Josey, S.A., Wunsch, C., 2004. Estimating air-sea fluxes of heat, freshwater, and momentum through global ocean data assimilation. Journal of Geophysical Research: Oceans 109. URL: https://agupubs.onlinelibrary.wiley.com/doi/abs/10.1029/2003JC002082, doi:10.1029/2003JC002082.

Stammer, D., Wunsch, C., Giering, R., Eckert, C., Heimbach, P., Marotzke, J., Adcroft, A., Hill, C.N., Marshall, J., 2002. Global ocean circulation during 1992–1997, estimated from ocean observations and a general circulation model. Journal of Geophysical Research: Oceans 107, 1–27. URL:

https://agupubs.onlinelibrary.wiley.com/doi/abs/10.1029/2001JC000888, doi:10.1029/2001JC000888.

Stommel, H., 1979. Determination of water mass properties of water pumped down from the Ekman layer to the geostrophic flow below. Proceedings of the National Academy of Sciences 76, 3051 LP – 3055. URL: http://www.pnas.org/content/76/7/3051.abstract, doi:10.1073/pnas.76.7.3051.

Teng, Y.C., Primeau, F.W., Moore, J.K., Lomas, M.W., Martiny, A.C., 2014. Global-scale variations of the ratios of carbon to phosphorus in exported marine organic matter. Nature Geoscience 7, 895–898. doi:10.1038/ngeo2303.

Trenberth, K.E., Fasullo, J.T., 2017. Atlantic meridional heat transports computed from balancing earth's energy locally. Geophysical Research Letters 44, 1919–1927. URL: https://agupubs.onlinelibrary.wiley.com/doi/abs/10.1002/2016GL072475, doi:10.1002/2016GL072475, arXiv:https://agupubs.onlinelibrary.wiley.com/doi/pdf/10

Trenberth, K.E., Large, W.G., J.G., O., 1989. A global ocean wind stress climatology based on ECMWF analyses.

USGS, 2009. Atmospheric mixing ratios of cfc-11, cfc-12, cfc-113, sf6. URL: http://water.usgs.gov/lab/software/air_curve/index.html.

Wang, W.L., Moore, J.K., Martiny, A.C., Primeau, F.W., 2019. Convergent estimates of marine nitrogen fixation. Nature 566, 205–211. URL: https://doi.org/10.1038/s41586-019-0911-2, doi:10.1038/s41586-019-0911-2.

Wanninkhof, R., 2014. Relationship between wind speed and gas exchange over the ocean revisited. Limnology and Oceanography: Methods 12, 351–362. URL: https://aslopubs.onlinelibrary.wiley.com/doi/abs/10.4319/lom.2014.12.351, doi:10.4319/lom.2014.12.351, arXiv:https://aslopubs.onlinelibrary.wiley.com/doi/pdf/

Waugh, D.W., Primeau, F., Devries, T., Holzer, M., 2013. Recent changes in the ventilation of the southern oceans. Science (New York, N.Y.) 339, 568–70. doi:10.1126/science.1225411.

Weber, T., Cram, J.A., Leung, S.W., DeVries, T., Deutsch, C., 2016. Deep ocean nutrients imply large latitudinal variation in particle transfer efficiency. Proceedings of the National Academy of Sciences 113, 8606–8611. URL: http://www.pnas.org/lookup/doi/10.1073/pnas.1604414113, doi:10.1073/pnas.1604414113, arXiv:arXiv:1408.1149.

Wenzel, M., Schröter, J., Olbers, D., 2001. The annual cycle of the global ocean circulation as determined by 4D VAR data assimilation. Progress in Oceanography 48, 73–119. URL: http://www.sciencedirect.com/science/article/pii/S0079661100000483, doi:https://doi.org/10.1016/S0079-6611(00)00048-3.

Williams, R.G., Marshall, J.C., Spall, M.A., 1995. Does Stommel's Mixed Layer "Demon" Work? Journal of Physical Oceanography 25, 3089–3102. doi:10.1175/1520-0485(1995)025<3089:DSMLW>2.0.CO;2.

Wunsch, C., 1996. The Ocean Circulation Inverse Problem. Cambridge University Press. doi:10.1017/CBO9780511629570.

Yu, L., Malanotte-Rizzoli, P., 1996. Analysis of the north atlantic climatologies using a combined ogcm/adjoint approach. Journal of Marine Research 54, 867–913. URL: https://www.ingentaconnect.com/content/jmr/jmr/1996/00000054/00000005/art00003, doi:doi:10.1357/0022240963213592.

Yu, L., Malanotte-Rizzoli, P., 1998. Inverse Modeling of Seasonal Variations in the North Atlantic Ocean. Journal of Physical Oceanography 28, 902–922. URL: https://doi.org/10.1175/1520-0485(1998)028<0902:IMOSVI>2.0.CO;2, doi:10.1175/1520-0485(1998)028¡0902:IMOSVI¿2.0.CO;2, arXiv:https://journals.ametsoc.org/jpo/article-pdf/28/5/902/4433096/1520-0485(19

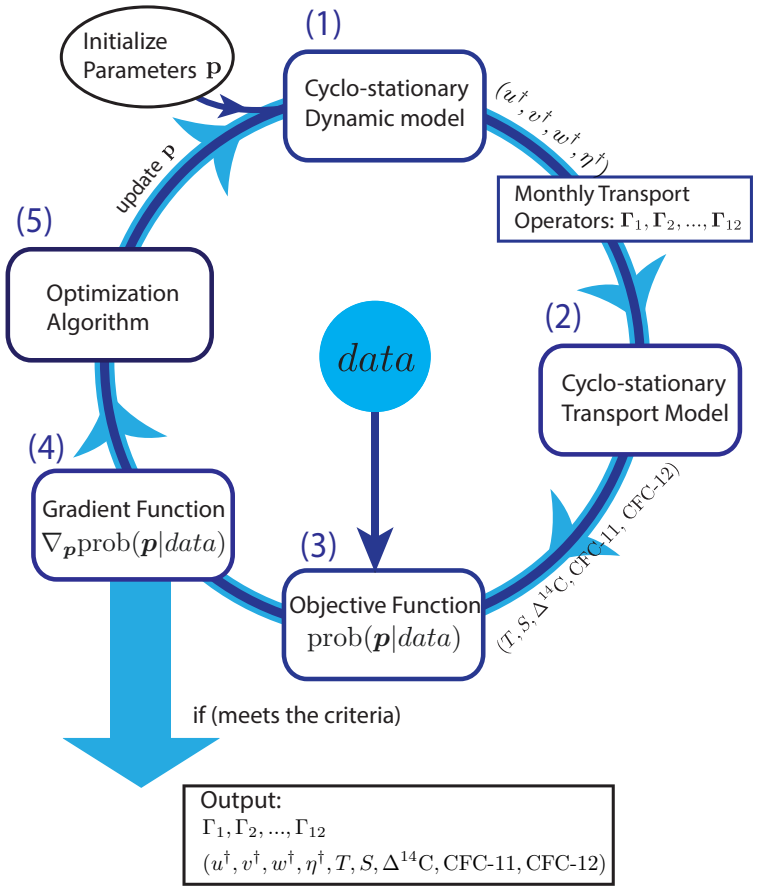

Figure 1: The workflow of the cyclo-stationary ocean circulation inverse model (CYCLOCIM).

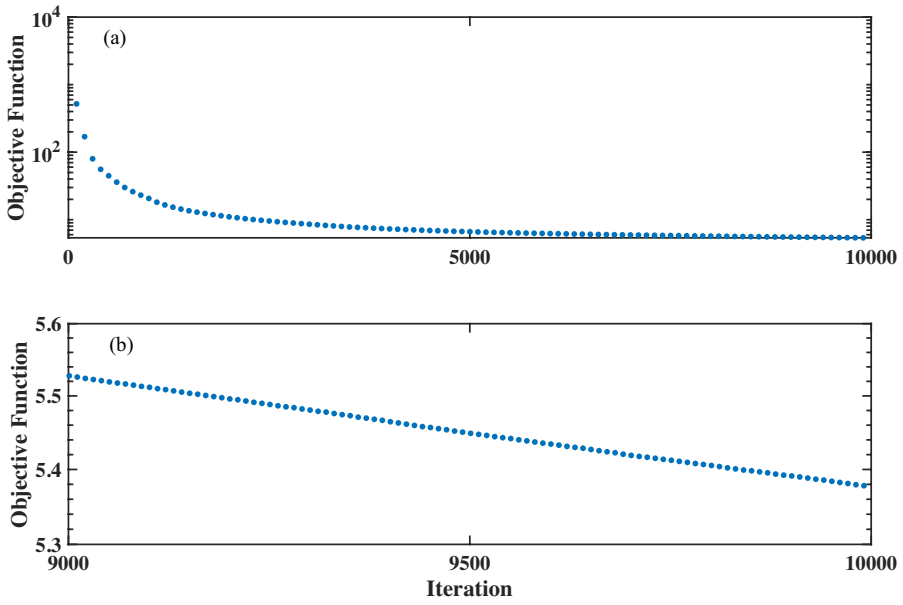

Figure 2: The evolution of the objective function for the $8^\circ \times 8^\circ \times 24$ model run in (a) first 10000 iterations (b) last 1000 iterations. Note that the contribution to the objective function from each tracer corresponds roughly to $\frac{1}{2}\chi_i^2/n_i$ for $i = 1, \cdots 5$, where χ_i^2 is the Chi-squared statistic for the i-th tracer and n_i is the number of observations of the i-th tracer. At the end of the optimization the value of the objective function, which includes both the log likelihood and log prior is ~ 5.4 which is close to the expected contribution of 2.5 from the likelihood alone based on the rule of thumb that each χ_i^2 term should be roughly equal to n_i.

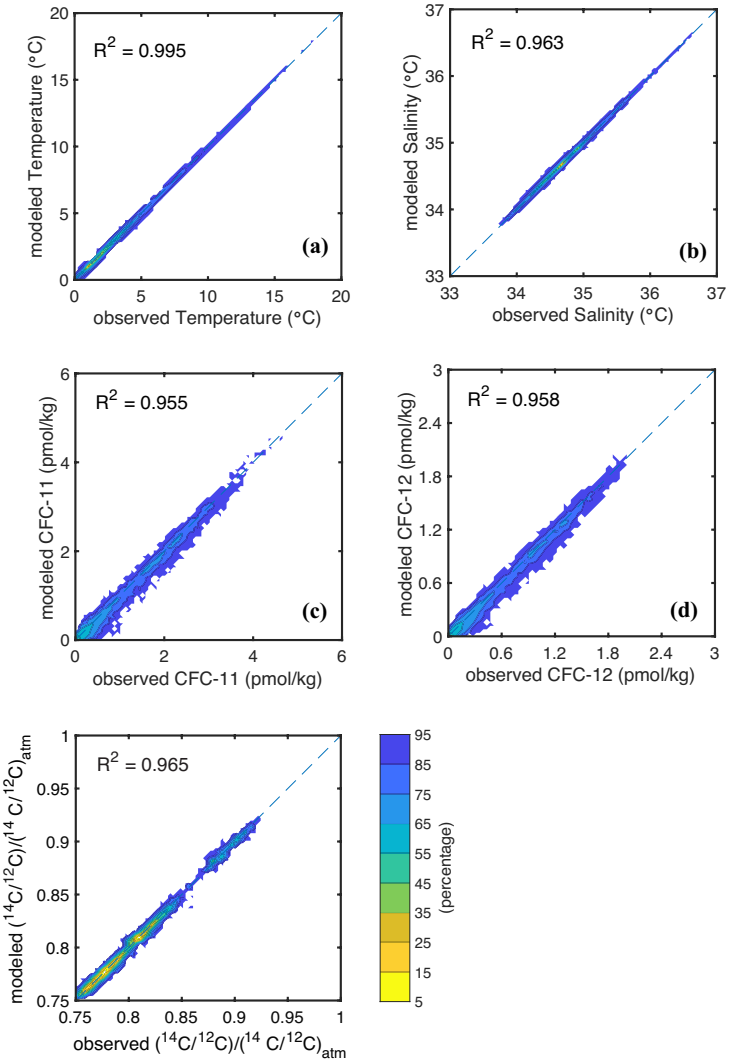

Figure 3: Joint distribution function for the gridbox-volume-weighted observed and modeled tracer concentrations: (a) potential temperature (b) salinity (c) CFC-11 (d) CFC-12 (e) Δ^{14}C, which are expressed in terms of the percentages of the cumulative distribution function. The Nth percentage is defined such that N% of the joint distribution lies inside N% contour. The joint distribution was estimated using the kernel density estimation method described in Botev et al. (2010) and modified to produce a volume weighted distribution (Primeau et al., 2013).

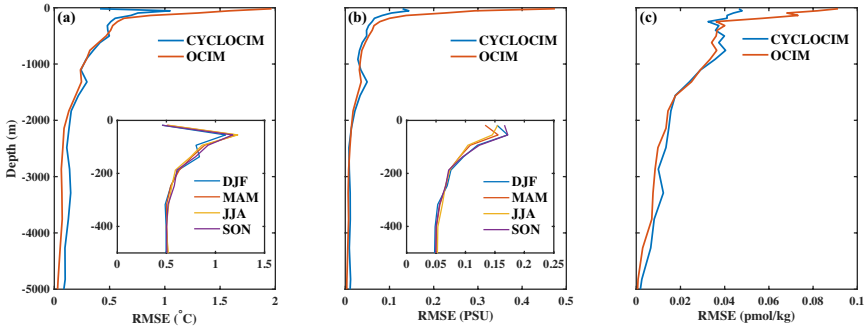

Figure 4: Horizontally-averaged root mean square error (RMSE) of (a) annual-mean potential temperature, (b) annual-mean salinity, and (c) CFC-11, computed from CYCLOCIM and OCIM. The subplot in (a) and (c) is the seasonal RMSE of potential temperature and salinity from CYCLOCIM in the upper ocean (0 - 500m).

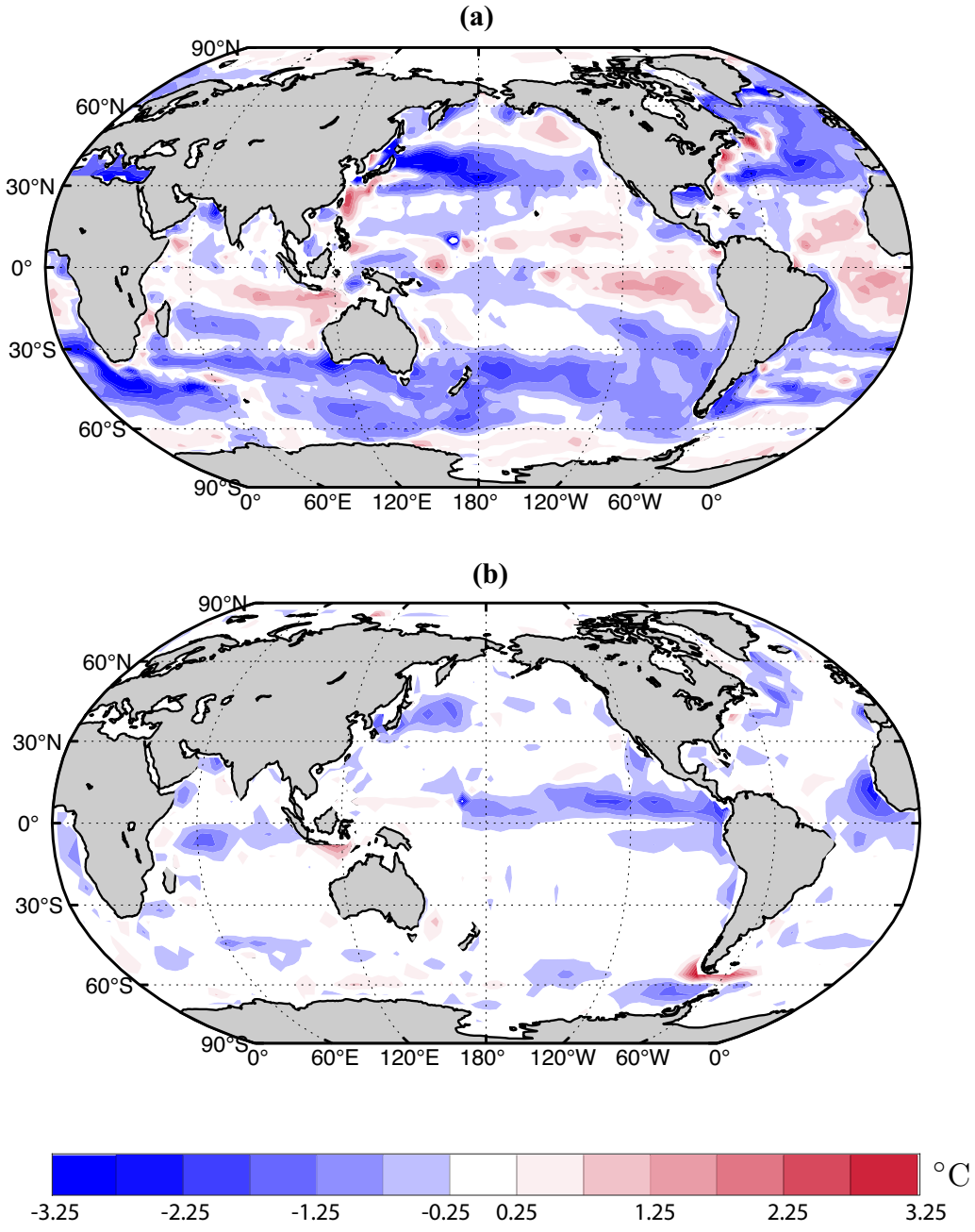

Figure 5: Difference between modeled and observed temperature in the upper 200m from OCIM (a) and CYCLOCIM (b) colored at 0.5 °C interval.

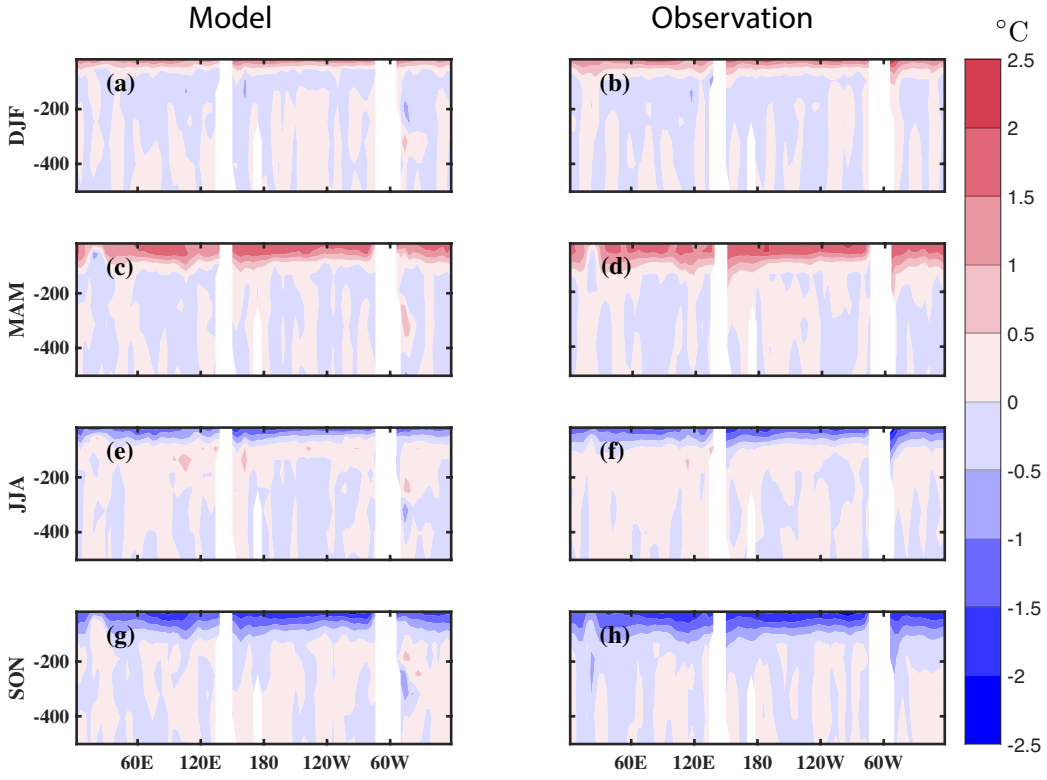

Figure 6: The longitude-depth section of the modeled potential temperature anomaly in comparison with the annual mean along 36°S in CYCLOCIM run from (a) December to February (DJF), (c) March to May (MAM), (e) June to August (JJA) and (g) September to November(SON), and the longitude-depth section of the observed potential temperature anomaly in comparison with the annual mean (b) December to February (DJF), (d) March to May (MAM), (f) June to August (JJA)and (h) September to November(SON).

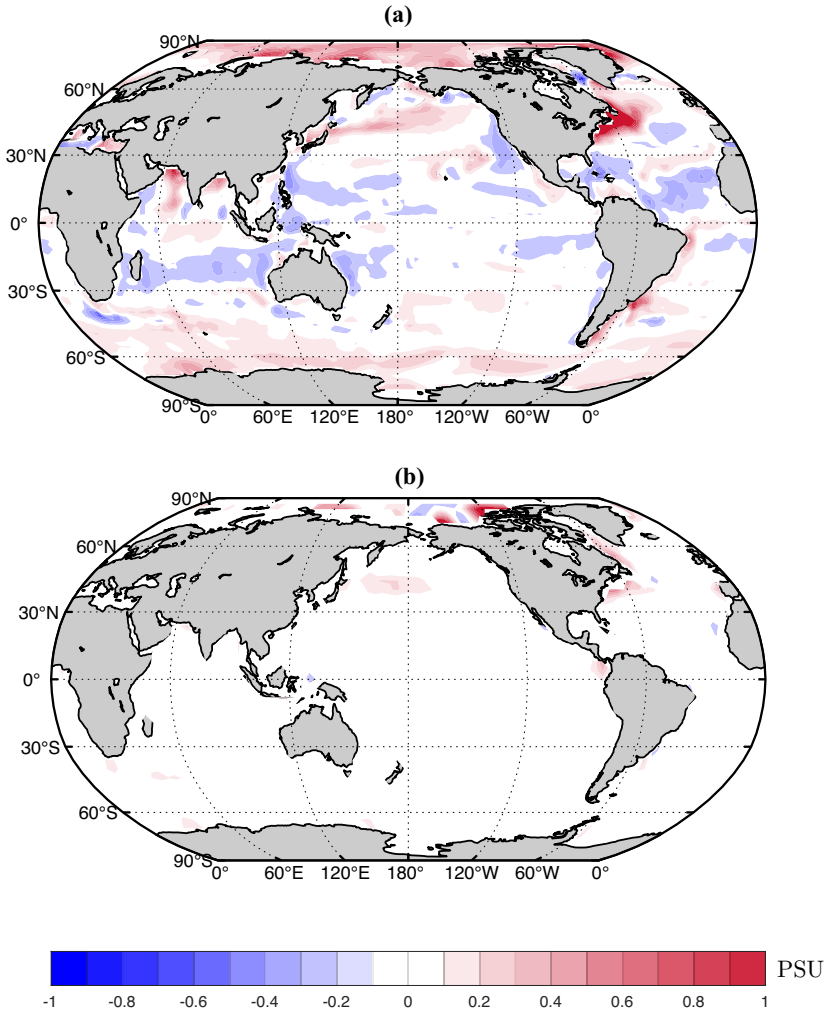

Figure 7: Difference between modeled and observed salinity in the upper 200m from OCIM (a) and CYCLOCIM (b), colored at 0.5 PSU interval.

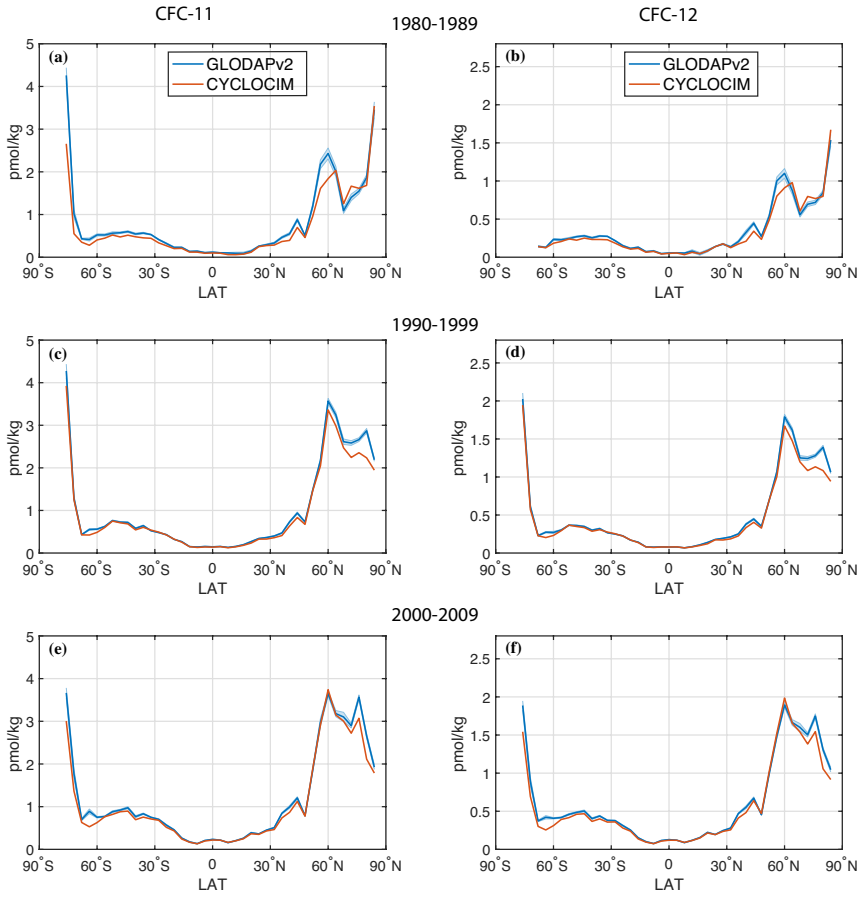

Figure 8: The zonal mean CFCs concentrations for CYCLOCIM compared to GLODAPv2 observations in three decades, panels (a and b) 1980-1989, (c and d) 1990-1999, (e and f) 2000-2009. The 3 panels on the left (a,c, and e) show CFC-11 and the three panels on the right (b,d, and f) show CFC-12. Only model grid boxes with observations in any given decade are used to construct the means. The corresponding number of observations in each decades is: 5991, 19042, 13313 for CFC-11 and 5320, 17962, 13742 for CFC-12. The blue shadow is one standard deviation of data in each latitude.

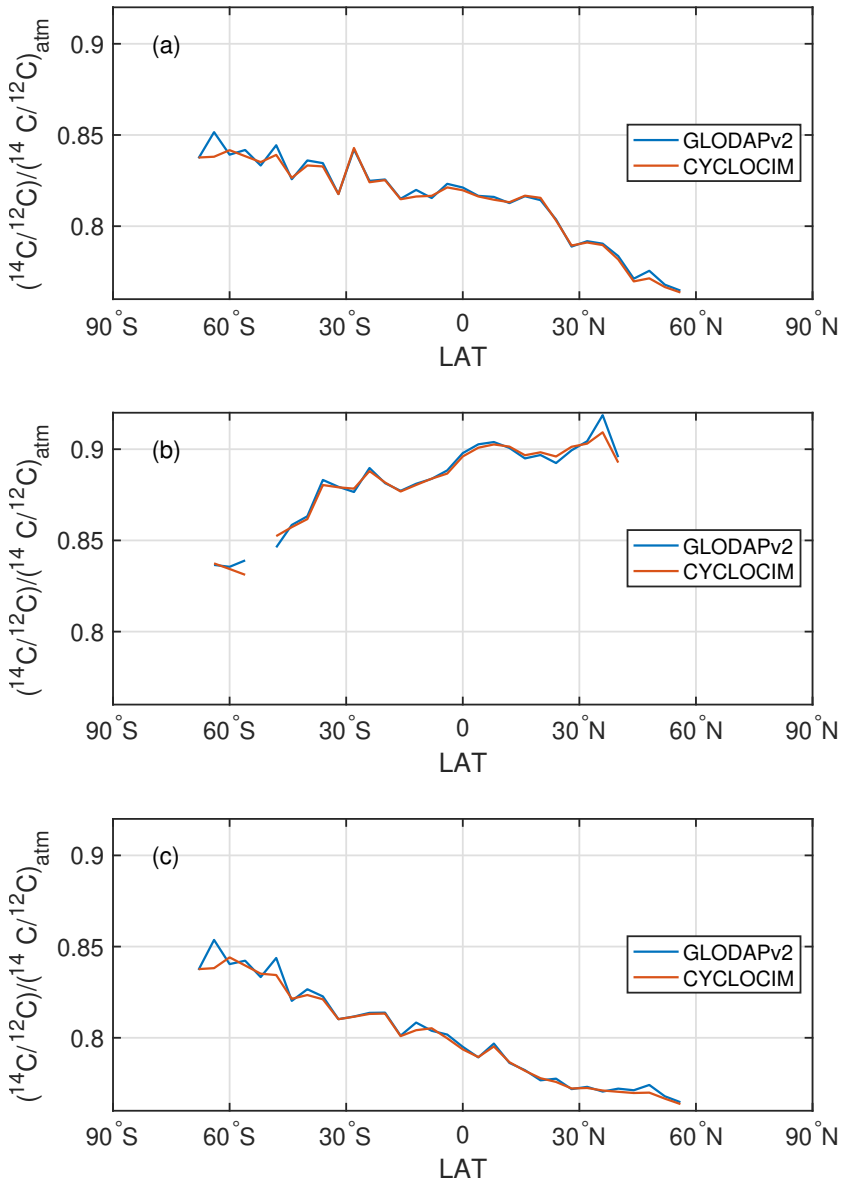

Figure 9: The zonal mean radiocarbon concentration relative to the pre-industrial atmosphere in CYCLOCIM compared to the GLODAPv2 observations. Only grid boxes with radiocarbon observations and no detectable CFCs are included in the basin averages. (a) global ocean, (b) Atlantic ocean and (c) Indo-Pacific ocean.

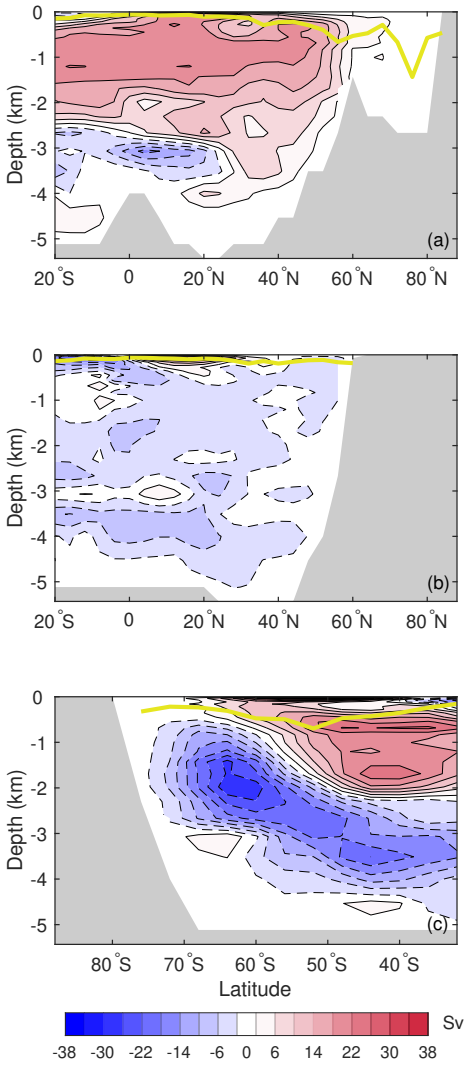

Figure 10: Climatogical mean meridional overturning circulation (MOC) stream function in three ocean basins for CYCLOCIM: (a) Atlantic Ocean (b) Pacific Ocean (c) Southern ocean. The contour interval corresponds to 4 Sv. Positive values indicate clockwise circulation, and negative values anti-clockwise circulation. The yellow line is the mean mixed layer depth at each basin.

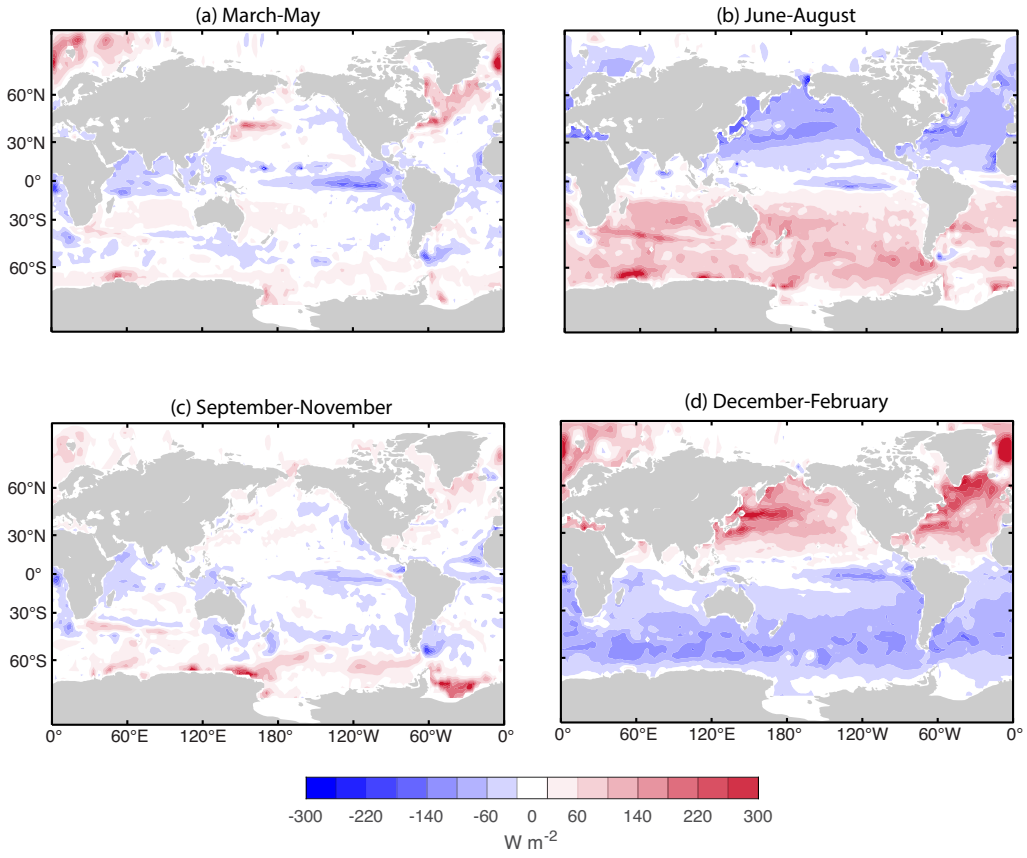

Figure 11: CYCLOCIM inferred global distribution of the seasonally-averaged climatiogical heat flux with 40 Wm^{-2} contour intervals in (a) spring (March-May) (b) summer (June-August) (c) Autumn (September-November) and (d) winter (December-February).

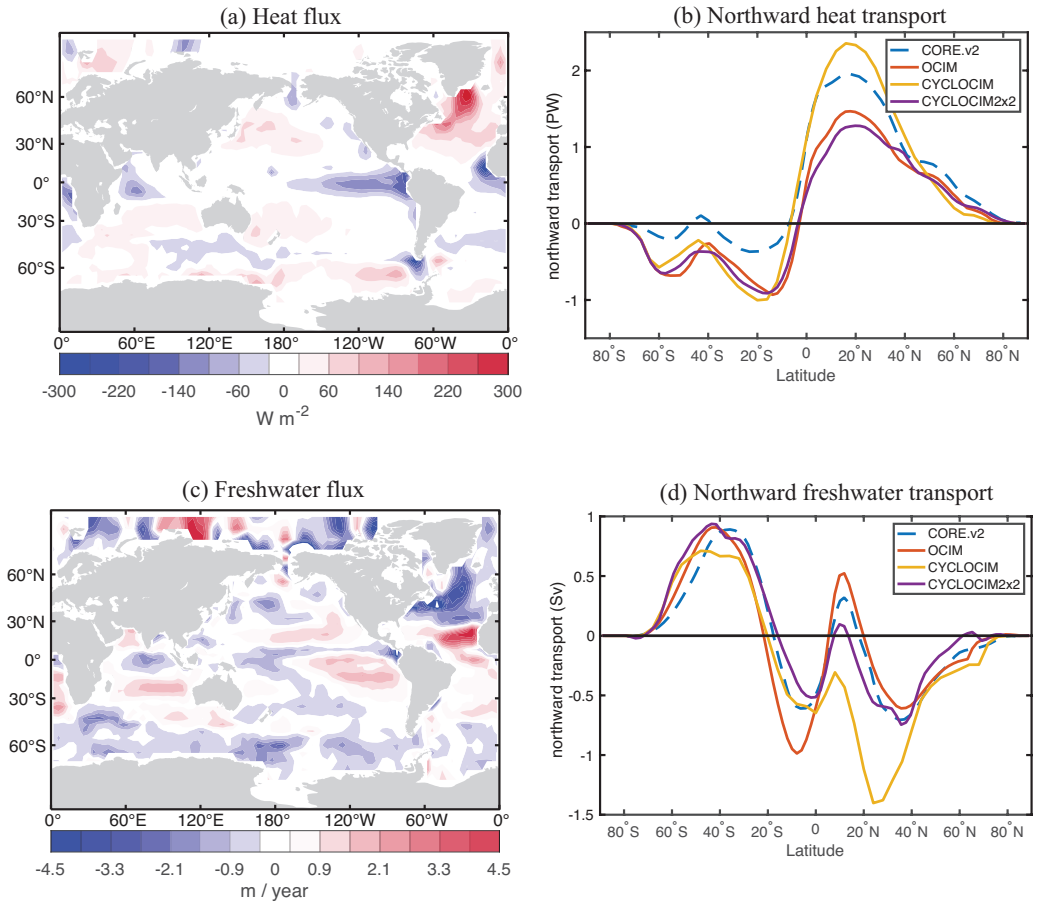

Figure 12: Global distribution of the annually-averaged climatiogical (a) heat flux with 40 Wm^{-2} contour intervals , and (c) freshwater flux with 0.6 m/year contour intervals inferred from the $4^\circ \times 4^\circ$ CYCLOCIM. The red colors indicate a flux out of the ocean and the blue colors indicate a flux into the ocean. Zonally averaged northward ocean (b) heat transports in PW and (d) freshwater transport in Sverdrup (Sv). Also indicated in panels (b) and (d) are the meridional transport estimates from CORE.v2 reproduced from Large and Yeager (2009), the OCIM-CTRL DeVries (2014) and an estimate from a not-fully-optimized version of the $2^\circ \times 2^\circ \times 24$ layer CYCLOCIM. We show the $2^\circ \times 2^\circ$ solution because it suggests that the implied meridional transport of heat and fresh water estimated from CYCLOCIM are quite sensitive to the horizontal resolution of the model.

Appendix A. Sensitivity experiments

Appendix A.1. Diffusivity

We have conducted three experiments similar to those presented by DeVries and Holzer (2019) for OCIM: one with the isopycnal diffusivity set to 2000 m^2/s (highISO), one with isopycnal diffusivity set to 600 m^2/s (lowISO), and one with high diapycnal diffusivity (highDIA) which increases from 10^{-5}m^2/s at the surface to 3^{-4}m^2/s at 5400 m. Each experiment starts with the optimal solution from the standard CYCLOCIM configuration and then run for 2000 iterations. Figure A.13 shows that the mean meridional overturning circulation in HighISO and HighDIA experiments are stronger than CYCLOCIM (Figure 10), whereas LowISO produces a weaker overturning circulation.

Appendix A.2. Restoring timescale

CYCLOCIM used a surface restoring timescale of $\tau = 30$ days for computing the surface fluxes of heat and freshwater (see Eq.14-16). We conducted two sensitivity experiments in which we halved and doubled the surface restoring time ($\tau = 15$ days and $\tau = 60$ days). Each sensitivity experiment started with the optimal parameters estimated from the standard CYCLOCIM configuration and was run for an additional 1500 iterations. The inferred heat and freshwater transports are shown in Figure A.14. The experiments show that the implied meridional transports are quite sensitivie to the choice of τ. This sensitivity suggests that in future work we will need to include the additional constraint on the surface fluxes of heat and freshwater from atmospheric reanalysis as we did previously for OCIM,(DeVries and Primeau, 2011). This sensitivity might also be due to the absence of a constraint on the dynamic topography from altimeter data, which was included in our previous state estimate using OCIM.

Appendix A.3. Parameter α

The optimal value of α used to scale the piston velocity in the air-sea gas exchange was 0.14 (cm/hr)/(m/s)^2 – a value that is significantly smaller than the value of 0.251 (cm/hr)/(m/s)^2 estimated by Wanninkhof (2014) for climatological winds. We therefore calculated the contribution to the objective function $\hat{f}$ (Eq. 28) from CFC-11 and CFC-12 misfits as a function of α. The sensitivity shown in the figure is performed holding all the other control parameters fixed at their optimized value. Taken at face value, these

results suggest that CYCLOCIM can provide a strong lower bound on α but only a weak upper bound. Any firm conclusion must await a more fully vetted state estimate, which is beyond the scope of the present article.

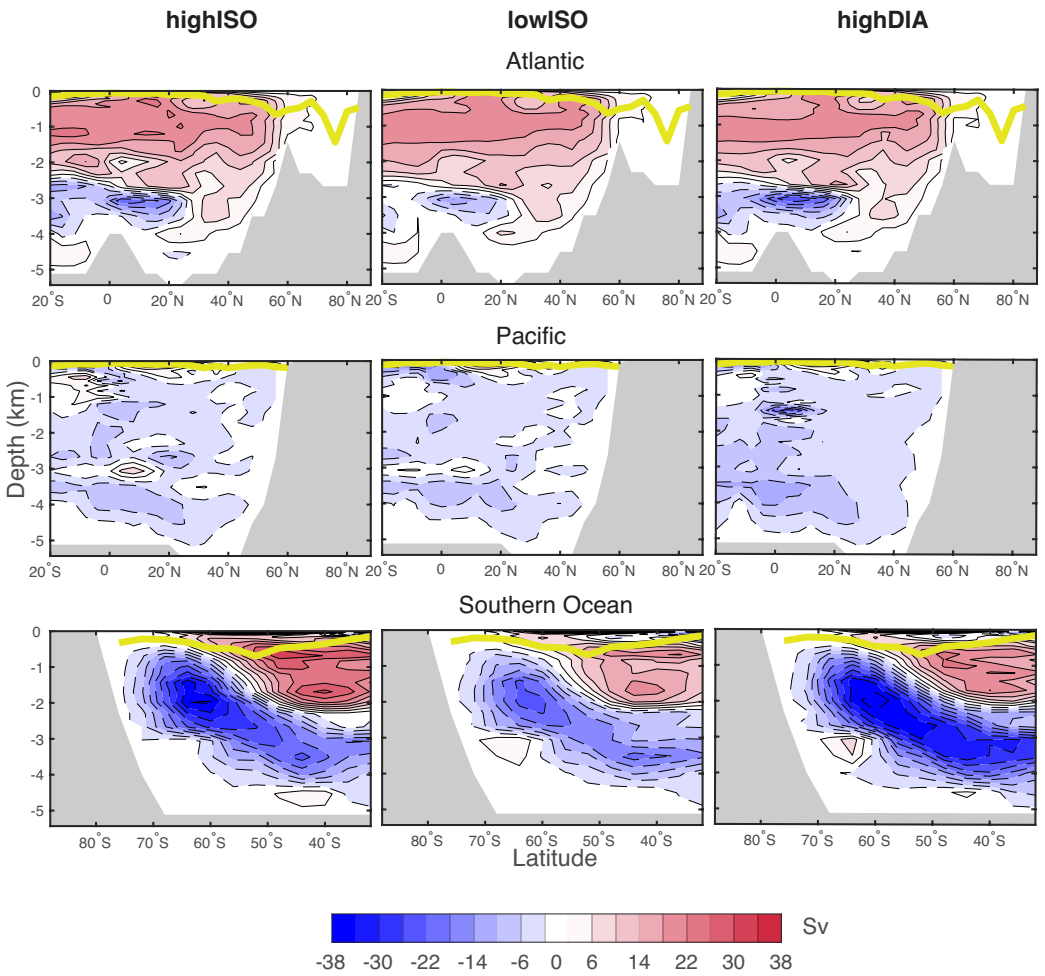

Figure A.13: Climatogical mean meridional overturning circulation (MOC) stream function in three ocean basins for CYCLOCIM: Atlantic Ocean, Pacific Ocean and Southern ocean. The three panel shows results from the experiment with high isopycnal diffusivity, low isopycnal diffusivity and high diapycnal diffusivity. The contour interval corresponds to 4 Sv. Positive values indicate clockwise circulation, and negative values anti-clockwise circulation. The yellow line is the mean mixed layer depth at each basin.

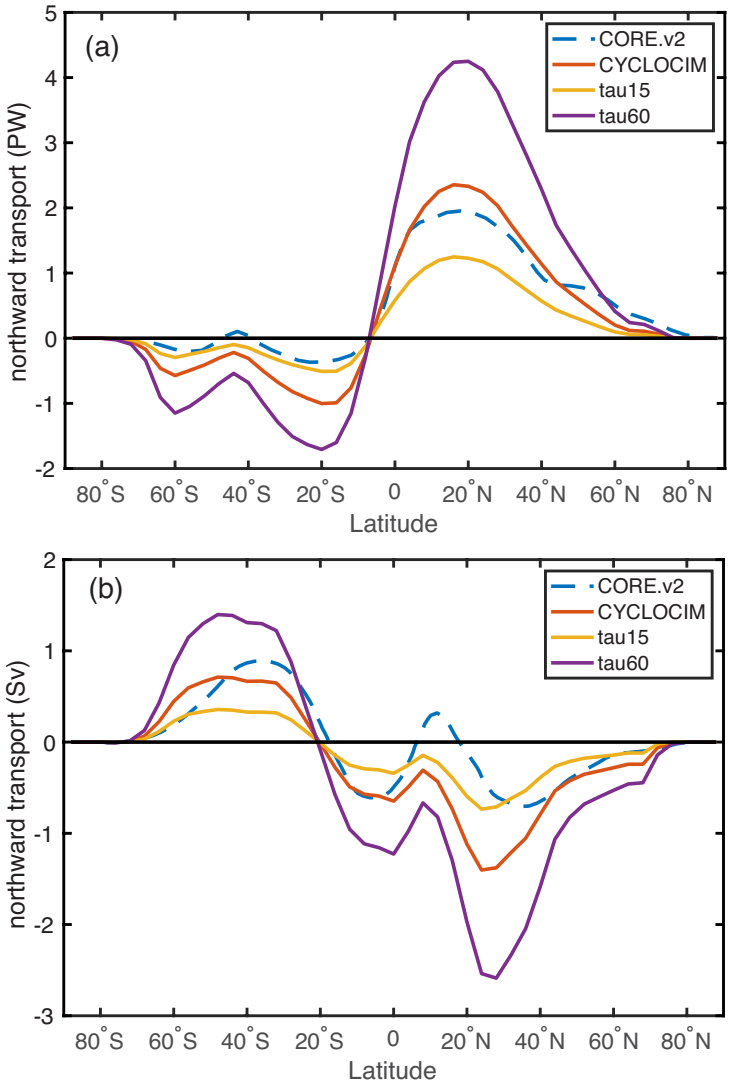

Figure A.14: Zonally averaged northward ocean (a) heat transports in PW and (b) freshwater transport in Sverdrup (Sv). The meridional transport estimates from CORE.v2 reproduced from Large and Yeager (2009), CYCLOCIM, the experiment with the restoring timescale $\tau = 15$ days and the experiment with the restoring timescale $\tau = 60$ days.

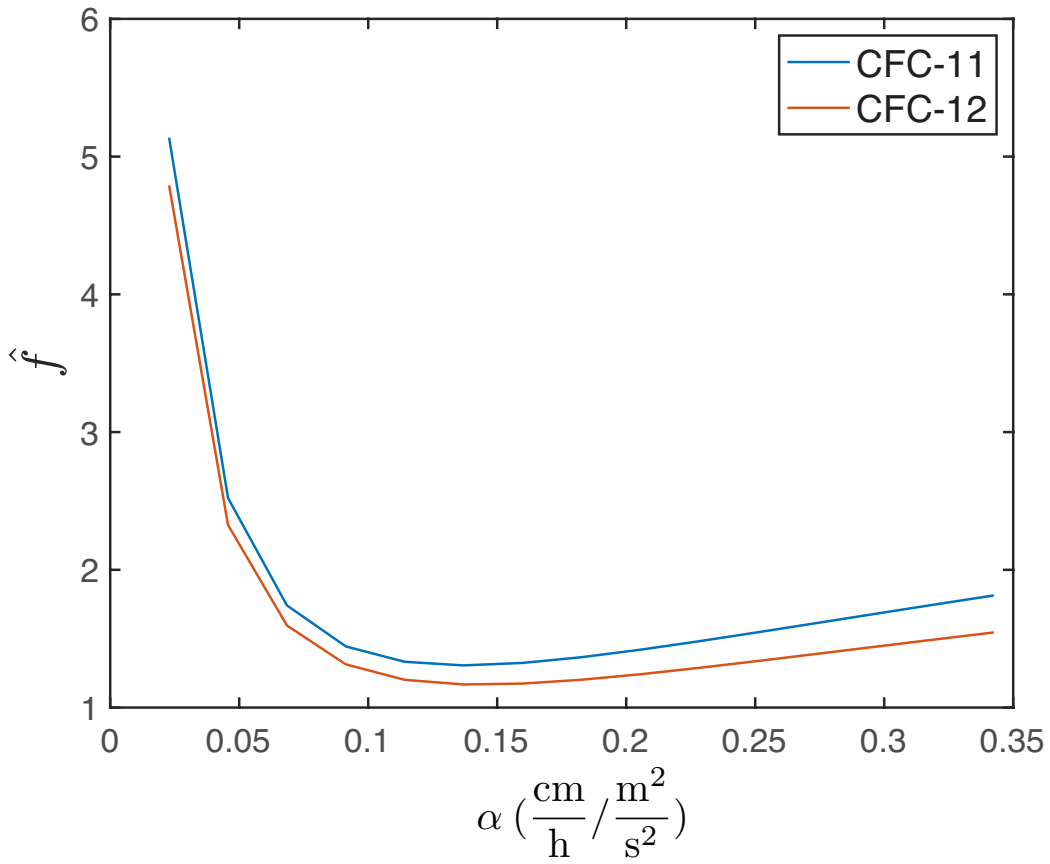

Figure A.15: The contribution to the objective function from CFC-11 and CFC-12 misfits as a function of α. The sensitivity shown in the figure is performed holding all the other control parameters fixed. The most probable value of α is 0.14. For references Wanninkhof (2014) estimates alpha to be 0.251 in the same units.